Chapter 13
Propagation Effects: Neutral Medium

The neutral gas in the atmosphere has a significant effect on signals passing through it. We are concerned with three types of effects. First, the large-scale structures in the media give rise to refractive effects. These effects, which can be analyzed in terms of geometrical optics and Fermat's principle, are the deflection of the radio waves and the change of the propagation velocity. Second, radiation can be absorbed. Finally, radiation can be scattered by the turbulent structure of the media. The phenomenon of scattering results in scintillation, or seeing.

In the troposphere, water vapor plays a particularly important role in radio propagation. The refractivity of water vapor is about 20 times greater in the radio range than in the near-infrared or optical regimes. The phase fluctuations in radio interferometers at centimeter, millimeter, and submillimeter wavelengths are caused predominantly by fluctuations in the distribution of water vapor. Water vapor is poorly mixed in the troposphere, and the total column density of water vapor cannot be accurately sensed from surface meteorological measurements. Uncertainties in the water vapor content are a serious limitation to the accuracy of VLBI measurements. Small-scale (< 1 km) fluctuations in water vapor distribution limit the angular resolution of connected-element interferometers in the absence of wavefront correction techniques. Furthermore, spectral lines of water vapor cause substantial absorption at frequencies above 100 GHz and usually render the troposphere highly opaque at frequencies between 1 and 10 THz (300 and 30 μm). Thus, any discussion of the neutral atmosphere must be primarily concerned with the effects of water vapor. Propagation in the neutral atmosphere from the point of view of radio communications is discussed by Crane (1981) and Bohlander et al. (1985).

Our interest in the propagation media arises because the media degrade interferometric measurements of radio sources. Alternately, observations of radio sources can be used to probe the characteristics of the propagation media. Radio interferometric measurements have been used widely for this purpose.

A.R. Thompson, J.M. Moran, and G.W. Swenson Jr., *Interferometry and Synthesis in Radio Astronomy*, Astronomy and Astrophysics Library,
DOI 10.1007/978-3-319-44431-4_13

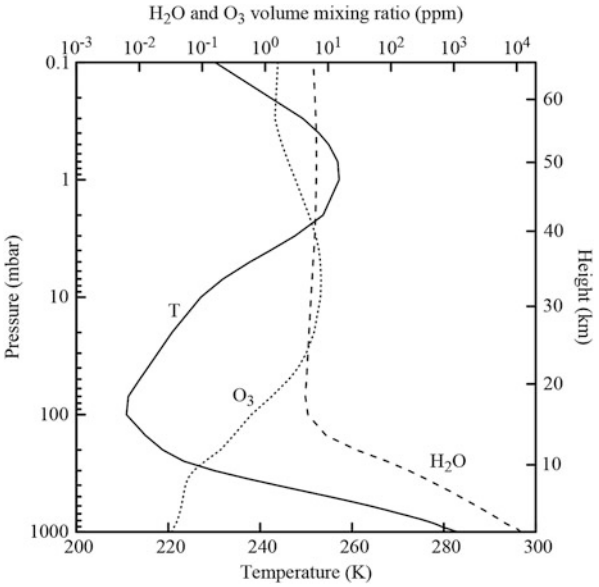

Fig. 13.1 Vertical profiles of temperature (solid line) and the water vapor (H_2O) (dashed line) and ozone (O_3) (dotted line) volume-mixing ratios, averaged over northern and southern midlatitudes for the period 2005–2014, compiled from the NASA Program for Modern-Era Retrospective Analysis for Research and Application (MERRA) reanalysis (Rienecker et al. 2011). The averaging captures diurnal and annual variations.

13.1 Theory

A temperature profile of the atmosphere is shown in Fig. 13.1. In the lowest part of the atmosphere, the temperature decreases monotonically from the surface at a rate of about 6.5 K km^{-1}, except for an occasional low-level inversion, until it reaches about 210 K at an altitude of approximately 12 km at midlatitudes. This lowermost layer is called the troposphere. Above 12 km, the temperature is relatively constant for a distance of about 10 km in the region called the tropopause. Above the tropopause, the temperature begins to rise with altitude in the stratosphere, due to the presence of ozone, reaching about 260 K at 45 km altitude. Above this level, the temperature drops with altitude through the mesosphere before rising again in the upper atmosphere, where the neutral atmosphere gives way to the ionosphere. Within the neutral atmosphere, the propagation of radio waves is most affected by the troposphere. Before discussing the refraction, absorption, and scattering of radio waves in the troposphere in detail, we introduce some basic physical concepts.

13.1.1 Basic Physics

Consider a plane wave propagating along the y direction in a uniform dissipative dielectric medium, as represented by the equation

$$\mathbf{E}(y,t) = \mathbf{E}_0 e^{j(kny - 2\pi\nu t)} \,, \tag{13.1}$$

where k is the propagation constant in free space and is equal to $2\pi\nu/c$, c is the velocity of light, and $\mathbf{E}_0$ is the electric field amplitude. n is the complex index of refraction, equal to $n_\mathrm{R} + jn_\mathrm{I}$. If the imaginary part of the index of refraction is positive, the wave will decay exponentially. The power absorption coefficient is defined as

$$\alpha = \frac{4\pi\nu}{c} n_\mathrm{I} \,. \tag{13.2}$$

Its units are m^{-1}. The propagation constant in the atmosphere is k multiplied by the real part of the index of refraction, which can be written

$$kn_\mathrm{R} = \frac{2\pi n\nu}{c} = \frac{2\pi\nu}{v_p} \,, \tag{13.3}$$

where $n = n_\mathrm{R}$ is the index of refraction when absorption is neglected, and v_p is the phase velocity. The phase velocity of the wave, c/n, is less than c by about 0.03% in the lower atmosphere. The extra time required to traverse a medium with index of refraction $n(y)$ compared with the time necessary to traverse the same distance in free space is

$$\Delta t = \frac{1}{c} \int (n-1)\, dy \,, \tag{13.4}$$

where we assume that the effect of the difference in physical length between the actual ray path and the straight-line path is negligible. The *excess* path length is defined as $c\Delta t$, or

$$\mathcal{L} = 10^{-6} \int N(y)\, dy \,, \tag{13.5}$$

where we have introduced the refractivity N, defined by $N = 10^6(n-1)$. Note that the concept of excess path length, which is used extensively in this chapter, does not represent an actual physical path.

A widely accepted expression for the radio refractivity is (Rüeger 2002)

$$N = 77.6898\frac{p_D}{T} + 71.2952\frac{p_V}{T} + 375463\frac{p_V}{T^2} \,, \tag{13.6}$$

where T is the temperature in kelvins, p_D is the partial pressure of the dry air, and p_V is the partial pressure of water vapor in millibars (1 mb = 100 newtons per square meter = 100 pascals = 1 hectopascal; 1 atmosphere = 1013 mb). The first two terms on the right side of Eq. (13.6) arise from the displacement polarizations of the gaseous constituents of the air (N_2, O_2, CO_2, and H_2O). The third term is due to the permanent dipole moment of water vapor. Equation (13.6) is formally known as the "zero-frequency" limit for the refractivity but is accurate to better than

1% for frequencies below 100 GHz. The contributions of dispersive components of refractivity associated with resonances below 100 GHz are very small. Between 100 and 1,000 GHz, the deviations from unity of the refractivity are more significant (see discussion in Sect. 13.1.4).

The refractivity can be expressed in terms of gas density, using the ideal gas law,

$$p = \frac{\rho RT}{\mathcal{M}} \,, \tag{13.7}$$

where p and ρ are the partial pressure and density of any constituent gas; R is the universal gas constant, equal to 8.314 J mol^{-1} K^{-1}; and $\mathcal{M}$ is the molecular weight, which for dry air in the troposphere is $\mathcal{M}_D = 28.96$ g mol^{-1} and for water vapor is $\mathcal{M}_V = 18.02$ g mol^{-1}. Thus, $p_D = \rho_D RT/\mathcal{M}_D$ and $p_V = \rho_V RT/\mathcal{M}_V$, where ρ_D and ρ_V are the densities of dry air and water vapor, respectively. Since the total pressure P is the sum of the partial pressures, and the total density ρ_T is the sum of the constituent densities, Eq. (13.7) can be written $P = \rho_T RT/\mathcal{M}_T$, where

$$\mathcal{M}_T = \left(\frac{1}{\mathcal{M}_D} \frac{\rho_D}{\rho_T} + \frac{1}{\mathcal{M}_V} \frac{\rho_V}{\rho_T} \right)^{-1} \,. \tag{13.8}$$

Substitution of the appropriate forms of Eq. (13.7) and the equation $\rho_D = \rho_T - \rho_V$ into Eq. (13.6) yields

$$N = 0.2228\rho_T + 0.076\rho_V + 1742\frac{\rho_V}{T} \,, \tag{13.9}$$

where ρ_T and ρ_V are in g m^{-3}. Since the second term on the right side of Eq. (13.9) is small with respect to the third term, it can be combined with the third term to give, for $T = 280$ K,

$$N \simeq 0.2228\rho_T + 1763\frac{\rho_V}{T} = N_D + N_V \,. \tag{13.10}$$

Equation (13.10) defines the dry and wet refractivities, N_D and N_V, respectively. These definitions are not universally followed in the literature. Note that N_D is proportional to the total density and therefore has a contribution due to the induced dipole moment of water vapor. Mean values of the distribution of the column density of water vapor around the world are shown in Fig. 13.2. For a discussion of climatology of water vapor, see Peixoto and Oort (1996).

The atmosphere is in hydrostatic equilibrium to a high degree of accuracy (Andrews 2000). A parcel of gas in static equilibrium between pressure and gravity obeys the equation

$$\frac{dP}{dh} = -\rho_T g \,, \tag{13.11}$$

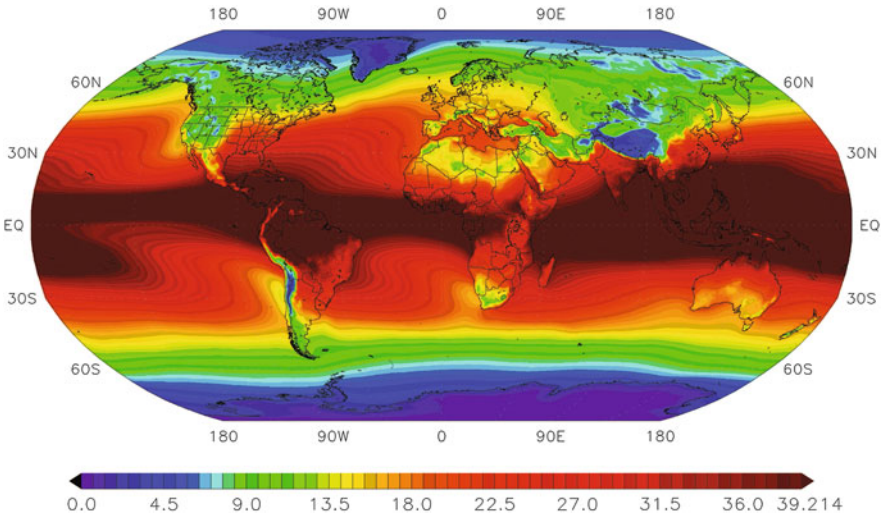

Fig. 13.2 Worldwide distribution of total water vapor content (w) based on satellite and ground-based observations over the ten-year period 2005–2014 in the framework of a global atmospheric model. The color scale denotes the column density in units of kg m^{-2} (equivalent to millimeters of precipitable water). Note that the resolution is not sufficient to show small localized areas of low water vapor, such as Mauna Kea. Data from the NASA MERRA Program. See Rienecker et al. (2011).

where g is the acceleration due to gravity, approximately equal to 980 cm s^{-2}, and h is the height above the Earth's surface. Using the ideal gas law, Eq. (13.7), we can integrate Eq. (13.11), assuming specific forms for the temperature profile and mixing ratio. If an isothermal atmosphere with constant mixing ratio is assumed, then ρ_T is an exponential function with a scale height of $RT/\mathcal{M}g \simeq 8.5$ km for 290 K, which is close to the observed scale height. Other models are described by Hess (1959). The excess path length caused by the dry component of refractivity does not depend on the height distribution of total density or temperature, but only on the surface pressure P_0, under conditions of hydrostatic equilibrium. If g is assumed to be constant with height, the surface pressure can be obtained by integrating Eq. (13.11),

$$P_0 = g \int_0^\infty \rho_T(h)\, dh \,. \tag{13.12}$$

From Eqs. (13.5), (13.10), and (13.12), the dry excess path length in the zenith direction is

$$\mathcal{L}_D = 10^{-6} \int_0^\infty N_D\, dh = AP_0 \,, \tag{13.13}$$

where $A = 77.6\, R/g\mathcal{M}_D = 0.228\,\text{cm mb}^{-1}$. Under standard conditions for which $P_0 = 1013\,\text{mb}$, the value of $\mathcal{L}_D$ is 231 cm.

Water vapor is not well mixed in the atmosphere and therefore is not well correlated with ground-based meteorological parameters (e.g., Reber and Swope 1972). On average, water vapor density has an approximately exponential distribution with a scale height of 2 km. This can be understood in the following way. The partial pressure and density of water vapor from Eq. (13.7) are related by

$$\rho_V = \frac{217 p_V}{T}\ (\text{g m}^{-3})\ . \tag{13.14}$$

The partial pressure of water vapor for saturated air, p_{VS}, at temperature T, obtained from the Clausius–Clapeyron equation (Hess 1959), can be approximated to an accuracy of better than 1% within the temperature range 240–310 K by the formula (Crane 1976)

$$p_{VS} = 6.11 \left(\frac{T}{273}\right)^{-5.3} e^{25.2(T-273)/T}\ (\text{mb})\ . \tag{13.15}$$

The relative humidity is p_V/p_{VS}. This approximation to the Clausius–Clapeyron equation is nearly an exponential function of temperature, dropping from 10.0 mb at 280 K to 3.7 (a factor of e^{-1}) at 266 K. For a lapse rate in temperature of 6 K km^{-1}, the profile of water vapor density is very close to an exponential function with a scale height of 2.5 km. For the purpose of this discussion, we adopt a simple model for the wet atmosphere as being isothermal with a scale height of 2.0 km, as is often observed.

The component of the path length resulting primarily from the permanent dipole moment of water vapor is, from Eq. (13.10),

$$\mathcal{L}_V = 1763 \times 10^{-6} \int_0^\infty \frac{\rho_V(h)}{T(h)}\, dh\ , \tag{13.16}$$

where the units of $\mathcal{L}_V$ are the same as those of h. Hence, for the approximation above, we obtain

$$\mathcal{L}_V \simeq 350\, \frac{\rho_{V0}}{T}\ \ (\text{cm}) \tag{13.17a}$$

or

$$\mathcal{L}_V = 7.6 \times 10^4 \frac{p_{V0}}{T^2}\ \ (\text{cm})\ , \tag{13.17b}$$

where ρ_{V0} and p_{V0} are the density and partial pressure of water vapor at the surface of the Earth, respectively. Hence, for $T = 280$ K, the path length is given by $\mathcal{L}_V = 1.26\rho_{V0} = 0.97 p_{V0}$.

The integrated water vapor density, or the height of the column of water condensed from the atmosphere, is given by

$$w = \frac{1}{\rho_w} \int_0^\infty \rho_V(h)\, dh \,, \tag{13.18}$$

where ρ_w is the density of water, 10^6 g m^{-3}. Hence, from Eq. (13.16), for an isothermal atmosphere at 280 K,

$$\mathcal{L}_V \simeq 6.3w \,. \tag{13.19}$$

This formula, which is widely used in the literature, is an excellent approximation for frequencies below 100 GHz. In the windows above 100 GHz, the ratio $\mathcal{L}_V/w$ can vary from 6.3 to about 8 (see Fig. 13.9 and associated discussion). The values of $\mathcal{L}_V$ under extreme conditions for a temperate, sea-level site can be calculated from the equations above. With $T = 303$ K (30 °C) and relative humidity = 0.8, we have $p_{V0} = 34$ mb, $\rho_{V0} = 24$ g m^{-3}, $w = 4.9$ cm, and $\mathcal{L}_V = 28$ cm. With $T = 258$ K (−15 °C) and relative humidity = 0.5, we have $p_{V0} = 1.0$ mb, $\rho_{V0} = 0.8$ g m^{-3}, $w = 0.15$ cm, and $\mathcal{L}_V = 1.1$ cm. The total zenith excess path length through the atmosphere is $\mathcal{L} \simeq \mathcal{L}_D + \mathcal{L}_V$, which, from Eqs. (13.13) and (13.19), is

$$\mathcal{L} \simeq 0.228P_0 + 6.3w \ \text{(cm)} \,, \tag{13.20}$$

where P_0 is in millibars, and w is in centimeters. Equation (13.20) is reasonably accurate for estimation purposes because the fractional variation in the temperature of the lower atmosphere, and in the scale height of water vapor, is usually less than 10%. However, it is usually not accurate enough to predict the path length to a small fraction of a wavelength at millimeter wavelengths.

13.1.2 Refraction and Propagation Delay

If the vertical distributions of temperature and water vapor pressure are known, then precise estimates of the angle of arrival and excess propagation time for a ray impinging on the atmosphere at an arbitrary angle can be computed by ray tracing. Here, we consider a few elementary cases in order to derive some simple analytic expressions. The simplest case is that of an interferometer in a uniform or plane-parallel atmosphere, as shown in Fig. 13.3. The refraction of the ray is governed by Snell's law, which is

$$n_0 \sin z_0 = \sin z \,, \tag{13.21}$$

where z is the zenith angle at the top of the atmosphere (where $n = 1$), and z_0 is the zenith angle at the surface (where $n = n_0$). The geometric delay for an

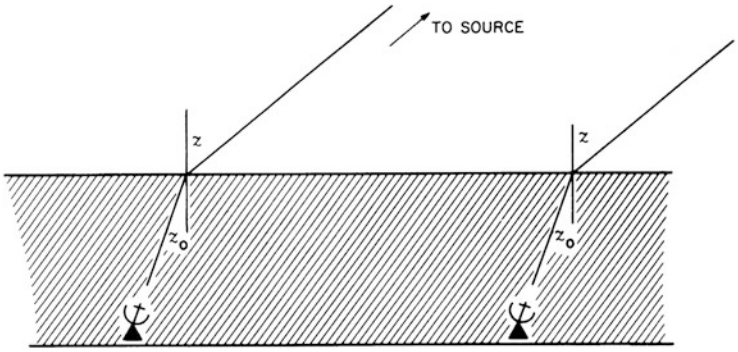

Fig. 13.3 Two-element interferometer with the atmosphere modeled as a uniform flat slab. The geometric delay is the same as it would be if the interferometer were in free space.

interferometer, as defined in Chap. 2, is

$$\tau_{\mathrm{g}} = \frac{n_0 D}{c} \sin z_0 = \frac{D}{c} \sin z \; . \tag{13.22}$$

τ_{g} can be calculated from the angle of arrival z_0 and the velocity of light at the Earth's surface c/n_0, or from z and the velocity of light in free space. Thus, if Earth curvature is neglected and the atmosphere is uniform, the resulting geometric delay is the same as the free-space value. The angle of refraction need only be calculated to ensure that the antennas track the source properly. The angle of refraction, $\Delta z = z - z_0$, can be written, using Eq. (13.21), as

$$\Delta z = z - \sin^{-1}\left(\frac{1}{n_0} \sin z\right) \; . \tag{13.23}$$

This equation can be expanded in a Taylor series in $n_0 - 1$, which to first order gives

$$\Delta z \simeq (n_0 - 1) \tan z \; . \tag{13.24}$$

Since $n_0 - 1 \simeq 3 \times 10^{-4}$ at the surface of the Earth, Eq. (13.24) can be written

$$\Delta z \; (\mathrm{arcmin}) \simeq \tan z \; . \tag{13.25}$$

The angle of refraction can also be calculated for more realistic cases. Ignore the curvature of the Earth, and consider the atmosphere to consist of a large number of plane-parallel layers numbered 0 through m, as shown in Fig. 13.4. Let the index of refraction at the surface be n_0, and at the top layer, $n_m = 1$. Applying Snell's law to

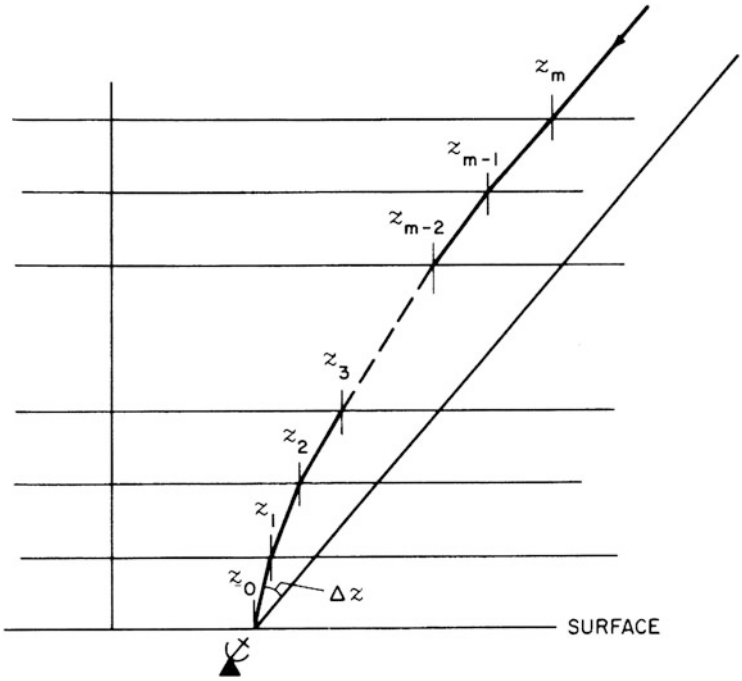

Fig. 13.4 The atmosphere modeled as a set of thin, uniform slabs. The angle of incidence on the topmost slab is z_m, which is equal to the free-space zenith angle z, and the angle of incidence at the surface is z_0. The total bending is $\Delta z = z - z_0$.

the various layers gives the following set of equations:

$$\begin{aligned} n_0 \sin z_0 &= n_1 \sin z_1 \\ n_1 \sin z_1 &= n_2 \sin z_2 \\ \vdots \qquad & \qquad \vdots \\ n_{m-1} \sin z_{m-1} &= \sin z \,, \end{aligned} \tag{13.26}$$

where $z = z_m$. From these equations, we see that $n_0 \sin z_0 = \sin z$. This result is identical to that for the homogenous case. Thus, regardless of the vertical distribution of the index of refraction, the angle of refraction is given by Eq. (13.21), where n_0 is the surface value of the index of refraction. This result can also be obtained by an elementary application of Fermat's principle. An interesting application of this result is that if $n_0 = 1$, as would be the case if the measuring device were in a vacuum chamber at the surface of the Earth, then there would be no net refraction; that is, $z_0 = z$.

For an atmosphere consisting of spherical layers, the angle of refraction is given by the formula (Smart 1977)

$$\Delta z = r_0 n_0 \sin z_0 \int_1^{n_0} \frac{dn}{n\sqrt{r^2 n^2 - r_0^2 n_0^2 \sin^2 z_0}} , \tag{13.27}$$

where r is the distance from the center of the Earth to the layer where the index of refraction is n and r_0 is the radius of the Earth. This result is derivable from Snell's law in spherical coordinates: $nr \sin z = \text{constant}$ (Smart 1977). For small zenith angles, expansion of Eq. (13.27) gives

$$\Delta z \simeq (n_0 - 1) \tan z_0 - a_2 \tan z_0 \sec^2 z_0 , \tag{13.28}$$

where a_2 is a constant. Equation (13.28) can also be written

$$\Delta z \simeq a_1 \tan z_0 - a_2 \tan^3 z_0 , \tag{13.29}$$

where $a_1 \simeq 56''$ and $a_2 \simeq 0.07''$ for a dry atmosphere under standard conditions (COESA 1976). The refraction at the horizon is about 0.46° (see Fig. 13.6). See Saastamoinen (1972a) for a more detailed treatment.

The differential delay induced in an interferometer by a horizontally stratified troposphere results from the difference in zenith angle of the source at the antennas. Consider two closely spaced antennas. If the excess path in the zenith direction is $\mathcal{L}_0$, then the excess path in other directions is approximately $\mathcal{L}_0 \sec z$. This approximation becomes inaccurate at large zenith angles. The difference in excess paths, $\Delta\mathcal{L}$, by first-order expansion, is

$$\Delta\mathcal{L} \simeq \mathcal{L}_0 \Delta z \frac{\sin z}{\cos^2 z} , \tag{13.30}$$

where Δz is the difference in zenith angles at the two antennas.

If the antennas are on the equator and the source has a declination of zero, then Δz is equal to the difference in longitudes, or approximately D/r_0, where D is the separation between antennas. For this case,

$$\Delta\mathcal{L} \simeq \frac{\mathcal{L}_0 D}{r_0} \frac{\sin z}{\cos^2 z} . \tag{13.31}$$

If $D = 10$ km, $\mathcal{L}_0 = 230$ cm, $r_0 = 6370$ km, and $z = 80°$, then $\Delta\mathcal{L}$ is 12 cm. The calculation of the difference in excess paths can be easily generalized as follows. Let $\mathbf{r}_1$ and $\mathbf{r}_2$ be vectors from the center of the Earth to each antenna. The geometric delay is $(\mathbf{r}_1 \cdot \mathbf{s} - \mathbf{r}_2 \cdot \mathbf{s})/c$, where $\mathbf{s}$ is the unit vector in the direction of the source.

Since $\cos z_1 = (\mathbf{r}_1 \cdot \mathbf{s})/r_0$ and $\cos z_2 = (\mathbf{r}_2 \cdot \mathbf{s})/r_0$, where z_1 and z_2 are the zenith angles at the two antennas, the geometric delay can be written

$$\tau_g = \frac{r_0}{c}(\cos z_1 - \cos z_2) \simeq \frac{r_0}{c}\Delta z \sin z \, . \tag{13.32}$$

Substitution of Δz from Eq. (13.32) into Eq. (13.30) yields an expression for the difference in excess path lengths, valid for short-baseline interferometers and moderate values of zenith angle:

$$\Delta\mathcal{L} \simeq \frac{c\tau_g \mathcal{L}_0}{r_0} \sec^2 z \, . \tag{13.33}$$

For very-long-baseline interferometers, the expression in Eq. (13.30) is not appropriate. The difference in excess path lengths is approximately $\Delta\mathcal{L} = \mathcal{L}_1 \sec z_1 - \mathcal{L}_2 \sec z_2$, where $\mathcal{L}_1$, $\mathcal{L}_2$, z_1, and z_2 are the excess zenith path lengths and the zenith angles at the two antennas. We now derive a more accurate expression for the excess path length to each antenna. The geometry is shown in Fig. 13.5. Assume the index of refraction to be exponentially distributed with a scale height h_0. The

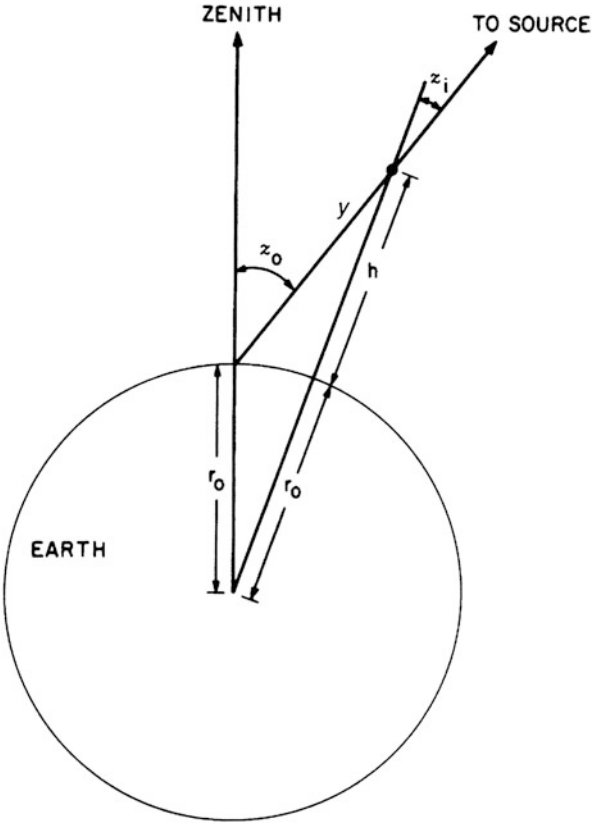

Fig. 13.5 Geometry for calculating the propagation delay, taking into account the sphericity of the Earth. The ray path along the y coordinate is assumed to be straight. The angle z_i is the zenith angle of the ray at height h. This angle is needed in the calculation of the excess path length through the ionosphere.

excess path length is

$$\mathcal{L} = 10^{-6} N_0 \int_0^\infty \exp\left(-\frac{h}{h_0}\right) dy \,, \tag{13.34}$$

where N_0 is the refractivity at the Earth's surface, h is the height above the surface, and dy is the differential length along the ray path. Bending of the ray is neglected. From the geometry of Fig. 13.5, $(h+r_0)^2 = r_0^2 + y^2 + 2r_0 y \cos z$. Using the quadratic formula and the second-order expansion $(1+\Delta)^{1/2} \simeq 1 + \Delta/2 - \Delta^2/8$, where $\Delta = (y^2 + 2yr_0 \cos z)/r_0^2$, one can show that

$$h \simeq y \cos z + \frac{y^2}{2r_0} \sin^2 z \,. \tag{13.35}$$

Therefore

$$\mathcal{L} \simeq 10^{-6} N_0 \int_0^\infty \exp\left(-\frac{y}{h_0} \cos z\right) \exp\left(-\frac{y^2}{2r_0 h_0} \sin^2 z\right) dy \,. \tag{13.36}$$

The argument of the rightmost exponential function in Eq. (13.36) is small, and this exponential function can be expanded in a Taylor series so that

$$\mathcal{L} \simeq 10^{-6} N_0 \int_0^\infty \exp\left(-\frac{y}{h_0} \cos z\right) \times \left(1 - \frac{y^2}{2r_0 h_0} \sin^2 z \cdots\right) dy \,. \tag{13.37}$$

Integration of Eq. (13.37) yields

$$\mathcal{L} \simeq 10^{-6} N_0 h_0 \sec z \left(1 - \frac{h_0}{r_0} \tan^2 z\right) \,. \tag{13.38}$$

Equation (13.38) can also be written

$$\mathcal{L} \simeq 10^{-6} N_0 h_0 \left[\left(1 + \frac{h_0}{r_0}\right) \sec z - \frac{h_0}{r_0} \sec^3 z\right] \,. \tag{13.39}$$

Thus, $\mathcal{L}$ is a function of odd powers of $\sec z$, whereas the bending angle, given in Eq. (13.29), is a function of odd powers of $\tan z$. Equations (13.38) and (13.39) both diverge as z approaches 90°. For $z = 90°$, Eq. (13.35) shows that $h \simeq y^2/2r_0$. Hence, for direct integration of Eq. (13.34), the excess path at the horizon is

$$\mathcal{L} \simeq 10^{-6} N_0 \sqrt{\frac{\pi r_0 h_0}{2}} \simeq 70 \mathcal{L}_0 \simeq 14 N_0 \ \text{(cm)} \tag{13.40}$$

for $r_0 = 6370$ km and $h_0 = 2$ km.

A model incorporating both the dry atmosphere with a scale height $h_D = 8$ km and the wet atmosphere with a scale height $h_V = 2$ km can be obtained by applying

Eq. (13.38) to both the dry and wet components using Eqs. (13.13) and (13.17). This result is

$$\mathcal{L} \simeq 0.228 P_0 \sec z\,(1 - 0.0013 \tan^2 z) + \frac{7.5 \times 10^4 p_{V0} \sec z}{T^2}(1 - 0.0003 \tan^2 z)\ . \tag{13.41}$$

More sophisticated models have been derived by Marini (1972), Saastamoinen (1972b), Davis et al. (1985), Niell (1996), and others. A comparison of the approximate formula of Eq. (13.41), a simple sec z model, and a ray-tracing solution is given in Fig. 13.6.

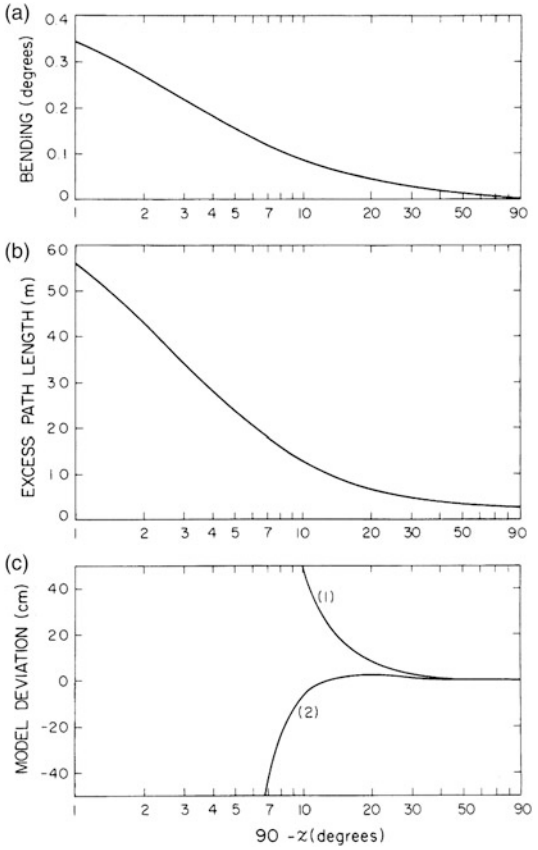

Fig. 13.6 (**a**) The bending angle vs. $90° - z$, where z is the zenith angle that the ray would have in the absence of refraction, calculated by a ray-tracing algorithm for a standard dry atmosphere (COESA 1976). (**b**) The excess path length vs. $90° - z$ calculated by a ray-tracing algorithm. The zenith excess path is 2.31 m. (**c**) Deviation between the excess path length and (1) the $\mathcal{L}_0 \sec z$ model and (2) the model of Eq. (13.41); in both cases, $\rho_{V0} = 0$, and the zenith excess path is the same as in (**b**).

13.1.3 Absorption

When the sky is clear, the principal sources of atmospheric attenuation are the molecular resonances of water vapor, oxygen, and ozone. The resonances of water vapor and oxygen are strongly pressure broadened in the troposphere and cause attenuation far from the resonance frequencies. A plot of the absorption vs. frequency is shown in Fig. 13.7. Below 30 GHz, absorption is dominated by the weak 6_{16}–5_{23} transition of H_2O at 22.2 GHz (Liebe 1969). Absorption by this line rarely exceeds 20% in the zenith direction. (See Appendix 13.1 for the history of research on this line.)

The oxygen lines in the band 50–70 GHz are considerably stronger, and no astronomical observations can be made from the ground in this band. An isolated oxygen line at 118 GHz makes observations impossible in the band 116–120 GHz. At higher frequencies, there is a series of strong water vapor lines at 183, 325, 380, 448, 475, 557, 621, 752, 988, and 1097 GHz and higher Liebe (1981). Observations can be made in the windows between these lines at dry locations, usually found at high altitudes. The physics of atmospheric absorption is discussed in detail by Waters (1976), and a model of absorption at frequencies below 1000 GHz is given by Liebe (1981, 1985, 1989). We are concerned here only with the phenomenology of absorption and its calibration. The absorption coefficient depends on the temperature, gas density, and total pressure. For example, the absorption coefficient for the

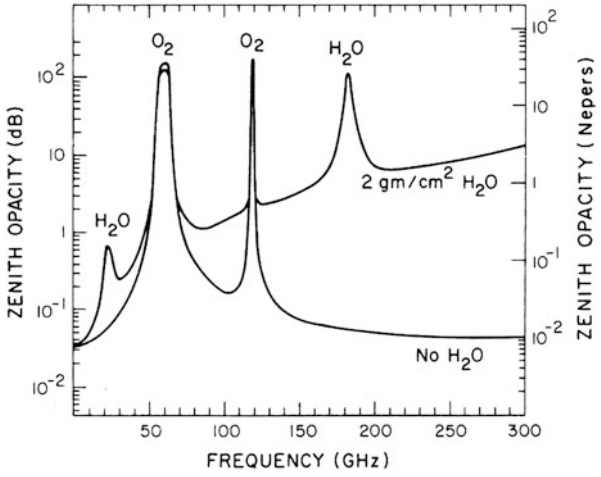

Fig. 13.7 Atmospheric zenith opacity. The absorption from narrow ozone lines has been omitted. Adapted from Waters (1976). For zenith opacity at frequencies above 300 GHz, see Liebe (1981, 1989). Note that 2 g cm^{-2} of H_2O corresponds to $w = 2$ cm.

22 GHz H_2O line can be written (Staelin 1966)

$$\alpha = \left(3.24 \times 10^{-4} e^{-644/T}\right) \frac{\nu^2 P \rho_V}{T^{3.125}} \left(1 + 0.0147 \frac{\rho_V T}{P}\right) \times \left[\frac{1}{(\nu - 22.235)^2 + \Delta\nu^2} + \frac{1}{(\nu + 22.235)^2 + \Delta\nu^2}\right] + 2.55 \times 10^{-8} \rho_V \nu^2 \frac{\Delta\nu}{T^{3/2}} \ (\mathrm{cm}^{-1}) \ . \tag{13.42}$$

Here, $\Delta\nu$ is approximately the half-width at half-maximum of the line in gigahertz, given by the equation

$$\Delta\nu = 2.58 \times 10^{-3} \left(1 + 0.0147 \frac{\rho_V T}{P}\right) \frac{P}{(T/318)^{0.625}} \ , \tag{13.43}$$

where ν is the frequency in gigahertz, T is the temperature in kelvins, P is the total pressure in millibars, and ρ_V is the water vapor density in grams per cubic meter. The lineshape specified by Eq. (13.42), the Van Vleck–Weisskopf profile, appears to fit the empirical data better than other theoretical profiles (Hill 1986). Other line parametrizations of the line profile are available, for example, Pol et al. (1998).

The intensity of a ray passing through an absorbing medium obeys the radiative transfer equation. We assume that the medium is in local thermodynamic equilibrium at temperature T and that scattering is negligible. In the domain where the Rayleigh–Jeans approximation to the Planck function is valid, so that the intensity is proportional to the brightness temperature, the equation of radiative transfer can be written (Rybicki and Lightman 1979)

$$\frac{dT_B}{dy} = -\alpha(T_B - T) \ , \tag{13.44}$$

where T_B is the brightness temperature and α is the absorption coefficient defined in Eqs. (13.2) and (13.42). The solution to Eq. (13.44) for radiation propagating along the y axis is

$$T_B(\nu) = T_{B0}(\nu) e^{-\tau_\nu} + \int_0^\infty \alpha(\nu, y) T(y) e^{-\tau'_\nu} \, dy \ , \tag{13.45}$$

where T_{B0} is the brightness temperature in the absence of absorption, including the cosmic background component,

$$\tau'_\nu = \int_0^y \alpha(\nu, y') \, dy' \ , \tag{13.46}$$

and

$$\tau_\nu = \int_0^\infty \alpha(\nu, y')\, dy' \ . \tag{13.47}$$

Here, y is the distance measured from the observer. τ_ν is called the *optical depth*, or *opacity*. The first term on the right side of Eq. (13.45) describes the absorption of the signal, and the second describes the emission contribution of the atmosphere. Equation (13.45) illustrates the fundamental law that an absorbing medium must also radiate. If $T(y)$ is constant throughout the medium, then Eq. (13.45) can be written

$$T_B(\nu) = T_{B0}(\nu) e^{-\tau_\nu} + T(1 - e^{-\tau_\nu}) \ . \tag{13.48}$$

The presence of absorption can have a very significant effect on system performance. If the receiver temperature is T_R, then the system temperature, which is the sum of T_R and the atmospheric brightness temperature (the effects of ground radiation being neglected), is

$$T_S = T_R + T_{\text{at}}(1 - e^{-\tau_\nu}) \ , \tag{13.49}$$

where T_{at} is the temperature of the atmosphere. In the absence of a source, the antenna temperature is taken as equal to the brightness temperature of the sky. Furthermore, if the brightness temperature scale is referenced to a point outside the atmosphere by multiplying the measurements of brightness temperature [see Eq. (13.48)] by e^{τ_ν}, then the effective system temperature is $T_S e^{\tau_\nu}$, or

$$T_S' = T_R e^{\tau_\nu} + T_{\text{at}}(e^{\tau_\nu} - 1) \ . \tag{13.50}$$

In effect, the atmospheric loss is modeled by an equivalent attenuator at the receiver input. Suppose that $T_R = 30\,\text{K}$, $T_{\text{at}} = 290\,\text{K}$, and $\tau_\nu = 0.2$; then the effective system temperature is 100 K. In such a situation, the atmosphere would degrade the system sensitivity by a factor of more than three. Note that the loss in sensitivity results primarily from the increase in system temperature rather than from the attenuation of the signal, which is only 20%. The emission from the atmosphere induces signals in spaced antennas that are uncorrelated and thus contributes only to the noise in the output of an interferometer.

The absorption can be estimated directly from measurements made with a radio telescope. In one technique introduced by Dicke et al. (1946), called the tipping-scan method, the opacity is determined from the atmospheric emission. If the antenna is scanned from the zenith to the horizon, the observed brightness temperature, in the absence of background sources, will depend on the zenith angle, since the opacity is proportional to the path length through the atmosphere, which varies approximately

as sec z. Thus, the atmospheric brightness temperature is

$$T_B = T_{\rm at}(1 - e^{-\tau_0 \sec z}) \ , \tag{13.51}$$

where τ_0 is the zenith opacity. When $\tau_0 \sec z \ll 1$,

$$T_B \simeq T_{\rm at} \tau_0 \sec z \ . \tag{13.52}$$

For narrow-beamed antennas, the antenna temperature is equal to the brightness temperature. For broad-beamed antennas, the antenna temperature is a zenith angle weighted version using Eq. (13.51). The opacity can be found from the slope of T_B plotted vs. sec z, assuming that $T_{\rm at}$ is the surface temperature. The accuracy of this method is affected by ground pickup through the sidelobes, which varies as a function of zenith angle.

The opacity can also be estimated from measurements of the absorption suffered by a radio source over a range of zenith angles. The observed antenna temperature on-source minus the antenna temperature off-source at the same zenith angle to remove the emission [see Eq. (13.48)] is

$$\Delta T_A = T_{S0} \, e^{-\tau_0 \sec z} \ , \tag{13.53}$$

where T_{S0} is the component of antenna temperature due to the source in the absence of the atmosphere. From Eq. (13.53),

$$\ln \Delta T_A = \ln T_{S0} - \tau_0 \sec z \ . \tag{13.54}$$

Thus, τ_0 can be found without knowledge of T_A if a sufficient range in sec z is covered. This method is affected by changes in antenna gain as a function of zenith angle.

Another technique, called the chopper-wheel method, is commonly used at millimeter wavelengths. A wheel consisting of alternate open and absorbing sections is placed in front of the feed horn. As the wheel rotates, the radiometer alternately views the sky and the absorbing sections and synchronously measures the difference in antenna temperature between the sky and the chopper wheel at temperature T_0. Thus, the on-source and off-source antenna temperatures are

$$\Delta T_{\rm on} = T_{S0} e^{-\tau_\nu} + T_{\rm at}(1 - e^{-\tau_\nu}) - T_0 \tag{13.55}$$

and

$$\Delta T_{\rm off} = T_{\rm at}(1 - e^{-\tau_\nu}) - T_0 \ . \tag{13.56}$$

Table 13.1 Empirical coefficients for estimating opacity from surface absolute humidity[a]

ν (GHz)	α_0 (nepers)	α_1 (nepers m^3 g^{-1})
15	0.013	0.0009
22.2	0.026	0.011
35	0.039	0.0030
90	0.039	0.0090

Source: Waters (1976).
[a]From the equation $\tau_0 = \alpha_0 + \alpha_1 \rho_{V0}$ fitted to opacity data derived from radiosonde measurements and measurements of surface absolute humidity, ρ_{V0} g m^{-3}.

These measurements can be combined to obtain T_0 and thereby eliminate the effect of atmospheric absorption. In the case in which $T_0 = T_{\text{at}}$,

$$T_{S0} = \left(\frac{\Delta T_{\text{off}} - \Delta T_{\text{on}}}{\Delta T_{\text{off}}} \right) T_0 \ . \tag{13.57}$$

When sensitivity is critical, the chopper wheel is used only to calibrate the output in the off-source position. $\Delta T_{\text{off}} - \Delta T_{\text{on}}$ in the numerator of Eq. (13.57) is then replaced by $T_{\text{off}} - T_{\text{on}}$. Measurement of T_{S0} provides the flux density of the source, which determines the visibility at the origin of the (u, v) plane.

The opacity can be estimated also from surface meteorological measurements when other data are not available. This method is not as accurate as the direct radiometric measurement techniques described above but has the advantage of not expending observing time. Waters (1976) has analyzed data on absorption vs. surface water vapor density for a sea-level site at various frequencies by fitting them to an equation of the form $\tau_0 = \alpha_0 + \alpha_1 \rho_{V0}$. The coefficients α_0 and α_1 are listed in Table 13.1.

13.1.4 Origin of Refraction

For practical reasons, we have discussed separately the effects of the propagation delay and the absorption in the neutral atmosphere. However, the delay and the absorption are intimately related because they are derived from the real and imaginary parts of the dielectric constant of the gas in the atmosphere. The real and imaginary parts of the dielectric constant are not independent but are related by the Kramers–Kronig relation, which is similar to the mathematical relation known as the Hilbert transform (Van Vleck et al. 1951; Toll 1956). We now discuss this relationship from the physical viewpoint of the classical theory of dispersion. From this analysis, it will become clear why the atmospherically induced delay is

essentially independent of frequency, even in the vicinity of spectral lines that cause significant absorption.

A dilute gas of molecules can be modeled as bound oscillators. In each molecule, an electron with mass m and charge $-e$ is harmonically bound to the nucleus, and the electron's motion is characterized by a resonance frequency ν_0 and damping constant $2\pi\Gamma$. The equation of motion with a harmonic driving force $-eE_0e^{-j2\pi\nu t}$ caused by the electric field of an electromagnetic wave can be approximated as

$$m\ddot{x} + 2\pi m\Gamma\dot{x} + 4\pi^2 m\nu_0^2 x = -eE_0e^{-j2\pi\nu t} , \tag{13.58}$$

where x is the displacement of the bound electron, E_0 and ν are the amplitude and frequency of the applied electric field, and the dots denote time derivatives. The steady-state solution has the form $x = x_0e^{-j2\pi\nu t}$, where

$$x_0 = \frac{eE_0/4\pi^2 m}{\nu^2 - \nu_0^2 + j\nu\Gamma} . \tag{13.59}$$

The magnitude of the dipole moment per unit volume, $\mathbf{P}$, is equal to $-n_m e x_0$, where n_m is the density of gas molecules. The dielectric constant[1] ε is equal to $1+\mathbf{P}/(\epsilon_0\mathbf{E})$, so that

$$\varepsilon = 1 - \frac{n_m e^2/4\pi^2 m\epsilon_0}{\nu^2 - \nu_0^2 + j\nu\Gamma} . \tag{13.60}$$

This classical model predicts neither the resonance frequency nor the absolute amplitude of the oscillation. A full treatment of the problem requires the application of quantum mechanics. The proper quantum-mechanical calculation for a system with many resonances yields a result that closely resembles Eq. (13.60) [e.g., Loudon (1983)]:

$$\varepsilon = 1 - \frac{n_m e^2}{4\pi^2 m\epsilon_0} \sum_i \frac{f_i}{\nu^2 - \nu_{0i}^2 + j\nu\Gamma_i} , \tag{13.61}$$

where f_i is the so-called oscillator strength of the ith resonance. The f_i values obey the sum rule, $\sum f_i = 1$.

[1] In this section and in Sect. 13.3, we use SI (System International) units, also known as rationalized MKS units. In this system, the constitutive relation between the displacement vector $\mathbf{D}$, the electric field vector $\mathbf{E}$, and the polarization vector $\mathbf{P}$ is $\mathbf{D} = \epsilon_0\mathbf{E} + \mathbf{P} = \epsilon\mathbf{E}$, where ϵ_0 is the permittivity of free space, and ϵ is the permittivity of the medium. The dielectric constant ε is ϵ/ϵ_0. A comparison of various systems of units and equations in electricity and magnetism can be found in Jackson (1999).

The dielectric constant ($\varepsilon = \varepsilon_R + j\varepsilon_I$) and index of refraction ($n = n_R + jn_I$) are connected by Maxwell's relation,

$$n^2 = \varepsilon \, . \tag{13.62}$$

Thus, $\varepsilon_R = n_R^2 - n_I^2$ and $\varepsilon_I = 2n_I n_R$. Since for a dilute gas $n_R \simeq 1$ and $n_I \ll 1$, we have $n_R \simeq \sqrt{\varepsilon_R}$ and $n_I \simeq \varepsilon_I/2$. Therefore, for a gas with a single resonance,

$$n_R \simeq 1 - \frac{n_m e^2(\nu^2 - \nu_0^2)/8\pi^2 m\epsilon_0}{(\nu^2 - \nu_0^2)^2 + \nu^2\Gamma^2} \tag{13.63}$$

and

$$n_I \simeq \frac{n_m e^2 \nu\Gamma/8\pi^2 m\epsilon_0}{(\nu^2 - \nu_0^2)^2 + \nu^2\Gamma^2} \, . \tag{13.64}$$

The resonance is usually sharp, that is, $\Gamma \ll \nu_0$, and the expressions for n_R and n_I can be simplified by considering their behavior in the vicinity of the resonance frequency ν_0, in which case

$$\nu^2 - \nu_0^2 = (\nu + \nu_0)(\nu - \nu_0) \simeq 2\nu_0(\nu - \nu_0) \, . \tag{13.65}$$

Thus

$$n_R \simeq 1 - \frac{2b(\nu - \nu_0)}{(\nu - \nu_0)^2 + \Gamma^2/4} \, , \tag{13.66}$$

and

$$n_I \simeq \frac{b\Gamma}{(\nu - \nu_0)^2 + \Gamma^2/4} \, , \tag{13.67}$$

where $b = n_m e^2/32\pi^2 m\epsilon_0 \nu_0$.

Equation (13.67) defines an unnormalized Lorentzian profile for n_I that is symmetric about frequency ν_0 and has a full width at half-maximum of Γ and a peak amplitude of $4b/\Gamma$. The function $n_R - 1$ is antisymmetric about frequency ν_0 and has extreme values of $\pm 2b/\Gamma$ at frequencies $\nu_0 \pm \Gamma/2$, respectively. The functions n_R and n_I are plotted in Fig. 13.8. Note that the peak deviation from unity in the real part of the index of refraction, Δn, is equal to one-half the peak value of n_I, denoted n_{Imax}. Thus, from Eq. (13.2), we see that the peak absorption coefficient, $\alpha_m = 4\pi n_{Imax}\nu_0/c$, is related to Δn by the formula

$$\Delta n = \frac{\alpha_m \lambda_0}{8\pi} \, , \tag{13.68}$$

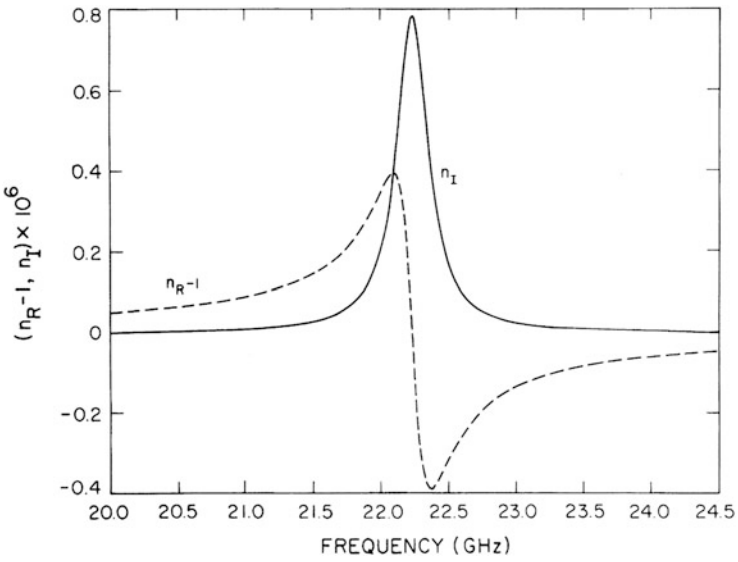

Fig. 13.8 Real and imaginary parts of the index of refraction vs. frequency for a single resonance, given by Eqs. (13.63) and (13.64). The case shown is for the 6_{16}–5_{23} transition in *pure* water vapor with $\rho_V = 7.5\,\mathrm{g\ m^{-3}}$. In the atmosphere at the standard sea-level pressure of 1013 mb, the line is broadened to about 2.6 GHz (Liebe 1969). For the curve $n_R - 1$, the peak deviation is Δn [see Eq. (13.68)], and the change in level passing through the line is δn [see Eq. (13.69)].

where λ_0 is the wavelength of the resonance, c/ν_0. The magnitude of the real part of the index of refraction is equal to the peak absorption over a distance of $\lambda_0/8\pi$. In addition, Eq. (13.66) shows that the real part of the index of refraction is not exactly symmetric about ν_0; that is, n_R tends to unity as ν tends to ∞, and n_R tends to $1 + 2b/\nu_0 = 1 + \Delta n\Gamma/\nu_0 = 1 + (\lambda_0\alpha_m/8\pi)(\Gamma/\nu_0)$ as ν tends to zero. Hence, the change δn in the asymptotic value of the index of refraction on passing through a resonance is given by

$$\delta n = \frac{\alpha_m \Gamma \lambda_0^2}{8\pi c}\ . \tag{13.69}$$

Thus, $\delta n/\Delta n = \gamma/\nu_0$, but unless the resonance is extremely strong, Δn and δn are both negligible. Consider the 22-GHz water vapor line. The attenuation in the atmosphere when $\rho_V = 7.5\,\mathrm{g\ m^{-3}}$ is $0.15\,\mathrm{dB\ km^{-1}}$, so $\alpha_m = 3.5 \times 10^{-7}\,\mathrm{cm^{-1}}$. Equation (13.68) then predicts that $\Delta n = 1.9 \times 10^{-8}$, or $\Delta N = 0.019$, which agrees with the value measured in the laboratory (Liebe 1969). For the same value of ρ_v, the contribution of all transitions of water vapor to the value of the index of refraction at low frequencies ($10^{-6}N_V$), from Eq. (13.10), is equal to 4.4×10^{-5}. Thus, the fractional change in refractivity near the 22-GHz line is only 1 part in 2500. The change in asymptotic level is even smaller. At sea level, $\Gamma = 2.6\,\mathrm{GHz}$ and $\delta n = 2.2 \times 10^{-8}$. The water vapor line at 557 GHz (the 1_{10}–1_{01} transition)

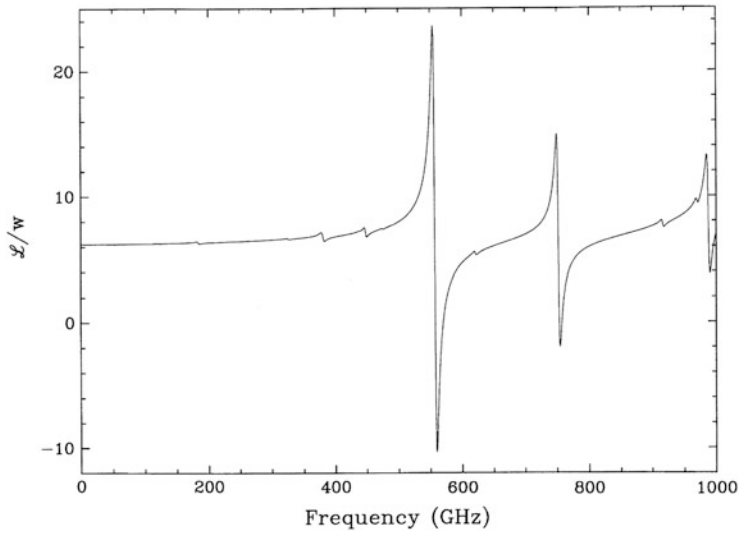

Fig. 13.9 The predicted excess path length due to water vapor per unit column density vs. frequency, from formulas by Liebe (1989) for $T = 270\,\mathrm{K}$ and $P = 750\,\mathrm{mb}$. From Sutton and Hueckstaedt 1996, reproduced with permission. © ESO.

has an absorption coefficient of 29,000 dB km^{-1}, or $0.069\,\mathrm{cm}^{-1}$. The values of Δn and δn are 1.44×10^{-6} and 0.7×10^{-6}, respectively. In the atmospheric windows above 400 GHz, where radio astronomical observations are possible only from very dry sites, the refractive index can be noticeably different from the value at lower frequencies. The normalized refractivity is shown in Fig. 13.9.

Equation (13.68) is an important result of very general validity. We derived it from a specific model [Eq. (13.58)] that led to an approximately Lorentzian profile for the absorption spectrum. In practice, line profiles are found to differ slightly from the Lorentzian form, and more sophisticated models are needed to fit them exactly. However, Eqs. (13.68) and (13.69) could be derived from the Kramers–Kronig relation.

The low-frequency value of the index of refraction, as given by Eq. (13.9), results from the contributions of all transitions at higher frequencies. Summing the contributions [see Eq. (13.69)] of many lines, each characterized by parameters Δn_1, Γ_i, α_{mi}, and ν_{0i}, we obtain the low-frequency value of the index of refraction:

$$n_S = 1 + \sum_i \frac{\alpha_{mi}\lambda_{0i}^2\Gamma_i}{8\pi c} = 1 + \sum_i \frac{\Delta n_i \Gamma_i}{\nu_{0i}} \,. \tag{13.70}$$

The water vapor molecule has a large number of strong rotational transitions in the band from 10 μm to 0.3 mm (from 30 THz to 1000 GHz). The atmosphere is

opaque through most of this region because of these lines, which contribute about 98% of the low-frequency refractivity. The remainder comes from the 557-GHz line.

Grischkowsky et al. (2013) show that the full theoretical calculation behind Eq. (13.70), based on Van Vleck–Weisskopf line shapes and incorporating all water lines from 22.2 GHz through 30 THz, gives agreement with the empirical expression for refractivity without any ad hoc corrections. Complete computer codes for the atmospheric absorption and refraction have been developed by Pardo et al. (2001a) and Paine (2016).

13.1.5 Radio Refractivity

A detailed discussion of the radio refractivity equation can be found in the report of a working group of the International Association of Geodesy (Rüeger 2002). Previous work on combining laboratory measurements includes Bean and Dutton (1966), Thayer (1974), Hill et al. (1982), and Bevis et al. (1994). From the classic work of Debye (1929), it can be shown that the refractivity of molecules with induced dipole transitions varies as pressure and T^{-1}, and the refractivity of molecules with permanent dipole moments varies as pressure and T^{-2}. The principal constituents of the atmosphere—oxygen molecules, O_2, and nitrogen molecules, N_2,—being homonuclear, have no permanent electric dipole moments. However, molecules such as H_2O and other minor trace constituents have permanent dipole moments. Thus, the general form of the refractivity equation is

$$N = \frac{K_1 p_D}{T \mathcal{Z}_D} + \frac{K_2 p_V}{T \mathcal{Z}_V} + \frac{K_3 p_V}{T^2 \mathcal{Z}_V} , \tag{13.71}$$

where p_D and p_V are the partial pressures of the dry air and water vapor; K_1, K_2, and K_3 are constants; and $\mathcal{Z}_D$ and $\mathcal{Z}_V$ are compressibility factors for dry-air gases and water vapor, which correct for nonideal gas behavior and deviate from unity in atmospheric conditions by less than 1 part in 10^3. These compressibility factors are given by Owens (1967) but are usually assumed to be equal to unity and their effects absorbed into the K coefficients.

The first and second terms in Eq. (13.71) are due to ultraviolet electronic transitions of the induced dipole type for dry-air molecules and water vapor, respectively, and the third term is due to the permanent dipole infrared rotational transitions of water vapor. The best values of the parameters are $K_1 = 77.6898$, $K_2 = 71.2952$, and $K_3 = 375463$, based on a weighted average of all available experimentally derived values before 2002, as presented by Rüeger (2002). These values were the result of working groups of the IUGG and the IAG. Thus, as in Eq. (13.6),

$$N = 77.6898 \frac{p_D}{T} + 71.2952 \frac{p_V}{T} + 375463 \frac{p_V}{T^2} . \tag{13.72}$$

The accuracy of this expression at the zero-frequency limit is conservatively estimated to be 0.02% for the p_D term and 0.2% for the p_V terms. We can rewrite Eq. (13.72) in terms of the total pressure ($P = p_D + p_V$) as

$$N = 77.7\frac{P}{T} - 6.4\frac{p_V}{T} + 375463\frac{p_V}{T^2} \,. \tag{13.73}$$

For temperatures around 280 K, the last two terms on the right side of Eq. (13.73) can be combined to give the well-known two-term *Smith–Weintraub equation* (Smith and Weintraub 1953) that has been widely used in the radio science community. Using the best available parameters in 1953, this equation is

$$N \simeq \frac{77.6}{T}\left(P + 4810\frac{p_V}{T}\right) \,. \tag{13.74}$$

The accuracy of Eqs. (13.73) and (13.74) at frequencies above zero can be improved by adding a small term that increases monotonically with frequency to account for the effect of the wings of the infrared transitions (see Fig. 13.9). Hill and Clifford (1981) show that because of this effect, the wet refractivity increases by about 0.5% at 100 GHz, and 2% at 200 GHz, over its value at low frequencies.

It is interesting to compare the refractivities at radio and optical wavelengths. The term proportional to T^{-2} is due to the infrared resonances of H_2O, because of its permanent dipole moment, and does not affect the optical refractivity. On the other hand, the terms proportional to T^{-1} arise from the induced dipole moments associated with resonances of oxygen and nitrogen and also water vapor in the ultraviolet. Hence, to a first approximation, we estimate the optical refractivity by omitting the permanent dipole term from Eq. (13.72) and obtain

$$N_{\text{opt}} \simeq 77.7\frac{p_D}{T} + 71.3\frac{p_V}{T} \,. \tag{13.75}$$

For precise work, Cox (2000) and Rüeger (2002) provide more accurate values for N_{opt} that include small terms having wavelength dependence to account for the effects of the wings of ultraviolet transitions that cause it to increase about 3% going from 1 to 0.3 μm. The ratio of the wet refractivity in the radio and optical regions is obtained by omitting the dry-air terms from Eqs. (13.72) and (13.75): $N_{V\text{rad}}/N_{V\text{opt}} \simeq 1 + 5830/T$. For $T \simeq 280$ K, this ratio is about equal to 22. Hence, water vapor plays a much more prominent role in propagation issues in radio than in optical astronomy.

13.1.6 Phase Fluctuations

In the radio region, the most important nonuniformly distributed quantity in the troposphere is the water vapor density. Variations in water vapor distribution in

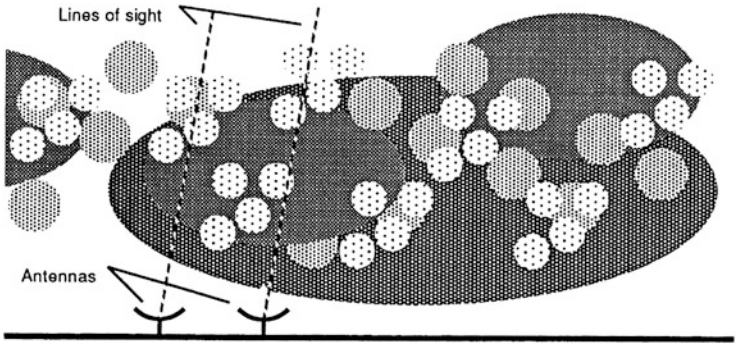

Fig. 13.10 A cartoon of a two-element interferometer beneath a tropospheric screen of water vapor irregularities of various sizes. The screen moves over the interferometer at a velocity component v_s parallel to the baseline. The distribution of these irregularities is important in designing the phase compensation schemes discussed in Sect. 13.2. Note that fluctuations with scale sizes larger than the baseline cover both antennas and do not affect the interferometer phase significantly. From Masson (1994a), courtesy of and © the Astronomical Society of the Pacific.

the troposphere that move across an interferometer cause phase fluctuations that degrade the measurements. In the optical region, variations in temperature, rather than in water vapor content, are the principal cause of phase fluctuations. The situation is depicted in Fig. 13.10. A critical dimension is the size of the first Fresnel zone, $\sqrt{\lambda h}$, where h is the distance between the observer and the screen. For $\lambda = 1\,\mathrm{cm}$ and $h = 1\,\mathrm{km}$, the Fresnel scale is about 3 m. The atmospherically induced phase fluctuations on this scale are very small ($\ll 1\,\mathrm{rad}$). In this case, the phase fluctuation can cause image distortion but not amplitude fluctuation (i.e., scintillation). This is known as the regime of weak scattering. Plasma scattering in the interstellar medium belongs to the regime of strong scattering, where the phenomena are considerably more complex (see Sect. 14.4).

The fluctuations along an initially plane wavefront that has traversed the atmosphere can be characterized by a so-called structure function of the phase. This function is defined as

$$D_\phi(d) = \langle [\Phi(x) - \Phi(x-d)]^2 \rangle \,, \tag{13.76}$$

where $\Phi(x)$ is the phase at point x, $\Phi(x-d)$ is the phase at point $x-d$, and the angle brackets indicate an ensemble average. In practical applications, the ensemble average must be approximated by a time average of suitable duration. We assume that D_ϕ depends only on the magnitude of the separation between the measurement points, that is, the projected baseline length d of the interferometer. The rms deviation in the interferometer phase is

$$\sigma_\phi = \sqrt{D_\phi(d)} \,. \tag{13.77}$$

For the sake of illustration, we assume a simple functional form for σ_ϕ given by

$$\sigma_\phi = \frac{2\pi a d^\beta}{\lambda} , \qquad d \le d_m , \tag{13.78a}$$

and

$$\sigma_\phi = \sigma_m , \qquad d > d_m , \tag{13.78b}$$

where a is a constant, and $\sigma_m = 2\pi a d_m^\beta/\lambda$. The form of Eqs. (13.78) is shown in Fig. 13.11a. This form can be derived by assuming a multiple-scale power-law model for the spectrum of the phase fluctuations. There is a limiting distance d_m beyond which fluctuations do not increase noticeably, a few kilometers, roughly the size of clouds. This limit is called the outer scale length of the fluctuations. Beyond this dimension, the fluctuations in the path lengths become uncorrelated.

First, consider an interferometer that operates in the domain of baselines shorter than d_m. The measured visibilities $\mathcal{V}_m$ are related to the true visibilities $\mathcal{V}$ by the

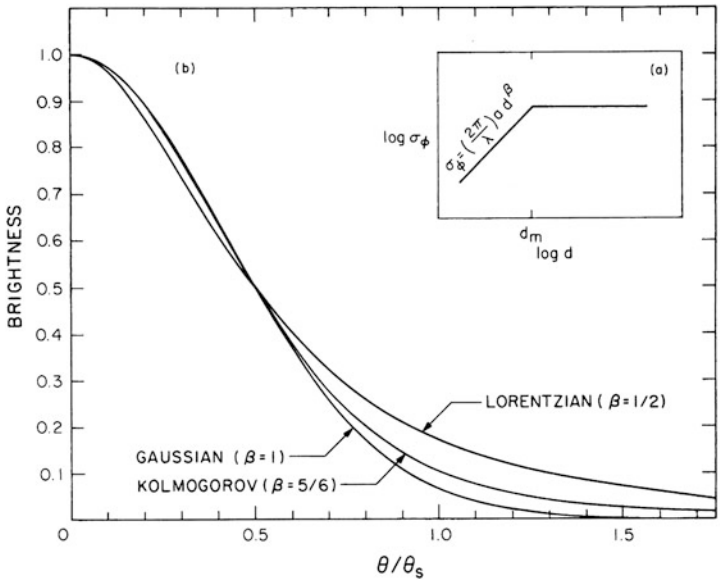

Fig. 13.11 (**a**) Simple model for the rms phase fluctuation induced by the troposphere in an interferometer of baseline length d given by Eqs. (13.78). (**b**) The point-source response function $\overline{w}_a(\theta)$ for various power-law models is obtained by taking the Fourier transform of the visibility in the regime $d < d_m$. The values of θ_s, the full width at half-maximum of $\overline{w}_a(\theta)$, for each model are: Gaussian ($\beta = 1$), $\sqrt{8 \ln 2}\, a$; modified Lorentzian ($\beta = \frac{1}{2}$), $1.53\pi\lambda^{-1}a^2$; and Kolmogorov ($\beta = \frac{5}{6}$), $2.75\lambda^{-1/5}a^{6/5}$. λ is the wavelength and a is the constant defined in Eq. (13.78a).

equation

$$\mathcal{V}_m = \mathcal{V} e^{j\phi} \ , \tag{13.79}$$

where $\phi = \Phi(x) - \Phi(x-d)$ is a random variable describing the phase fluctuations introduced by the atmosphere. If we assume ϕ is a Gaussian random variable with zero mean, then the expectation of the visibility is

$$\langle \mathcal{V}_m \rangle = \mathcal{V} \langle e^{j\phi} \rangle = \mathcal{V} e^{-\sigma_\phi^2/2} = \mathcal{V} e^{-D_\phi/2} \ . \tag{13.80}$$

Consider the conceptually useful case in which $\beta = 1$. It would arise in an atmosphere consisting of inhomogeneous wedges of scale size larger than the baseline. In this case, σ_ϕ is proportional to d, and the constant a is dimensionless. Substituting Eq. (13.78a) into Eq. (13.80) yields

$$\langle \mathcal{V}_m \rangle = \mathcal{V} e^{-2\pi^2 a^2 q^2} \ , \tag{13.81}$$

where $q = \sqrt{u^2 + v^2} = d/\lambda$. On average, therefore, the measured visibility is the true visibility multiplied by an atmospheric weighting function $w_a(q)$ given by

$$w_a(q) = e^{-2\pi^2 a^2 q^2} \ . \tag{13.82}$$

In the image plane, the derived map is the convolution of the true source distribution and the Fourier transform of $w_a(q)$, which is

$$\overline{w}_a(\theta) \propto e^{-\theta^2/2a^2} \ , \tag{13.83}$$

where θ is here the conjugate variable of q. The full width at half-maximum of $\overline{w}_a(\theta)$ is θ_s, given by

$$\theta_s = \sqrt{8 \ln 2}\, a \ . \tag{13.84}$$

Thus, the resolution is degraded because the derived map is convolved with a Gaussian beam of width θ_s (in addition to the effects of any other weighting functions, as described in Sect. 10.2.2). θ_s is the seeing angle. Images with finer resolution than θ_s can often be obtained by use of adaptive calibration procedures described in Sect. 11.3. Now, from Eq. (13.78a), we obtain

$$a = \frac{\sigma_\phi \lambda}{2\pi d} = \frac{\sigma_d}{d} \ , \tag{13.85}$$

where $\sigma_d = \sigma_\phi \lambda / 2\pi$ is the rms uncertainty in path length. Thus, we obtain

$$\theta_s = 2.35 \frac{\sigma_d}{d} \ \text{(radians)} \ . \tag{13.86}$$

Since σ_d/d is constant, θ_s is independent of wavelength. This independence results from the condition $\beta = 1$ in Eq. (13.78a). For the radio regime, σ_d is about 1 mm on a baseline of 1 km, so $a \simeq 10^{-6}$ and $\theta_s \simeq 0.5''$. Let d_0 be the baseline length for which $\sigma_\phi = 1$ rad. From Eq. (13.85), we see that Eq. (13.84) can be written in the form

$$\theta_s = \frac{\sqrt{2\ln 2}}{\pi}\frac{\lambda}{d_0} \simeq 0.37\frac{\lambda}{d_0} . \tag{13.87}$$

For the case in which β is arbitrary, we find $\overline{w}_a(\theta)$ by substituting Eq. (13.78a) into Eq. (13.80) and writing the two-dimensional Fourier transform as a Hankel transform (Bracewell 2000). Thus

$$\overline{w}_a(\theta) \propto \int_0^\infty \exp\left[-2\pi^2 a^2 \lambda^{2(\beta-1)} q^{2\beta}\right] J_0(2\pi q\theta)\, q\, dq , \tag{13.88}$$

where J_0 is the Bessel function of order zero and a has dimensions $\mathrm{cm}^{(1-\beta)}$. In general, $\overline{w}_a(\theta)$ cannot be evaluated analytically. However, by making appropriate substitutions in Eq. (13.88), it is easy to show that $\theta_s \propto a^{1/\beta}\lambda^{(\beta-1)/\beta}$. A case that can be treated analytically is the one for which $\beta = \frac{1}{2}$. In this case, we obtain (Bracewell 2000, p. 338)

$$\overline{w}_a(\theta) \propto \frac{1}{[\theta^2 + (\pi a^2/\lambda)^2]^{3/2}} , \tag{13.89}$$

which represents a Lorentzian profile raised to the 3/2 power and has very broad skirts. The full width at half-maximum of $\overline{w}_a(\theta)$ is

$$\theta_s = \frac{1.53\pi a^2}{\lambda} , \tag{13.90}$$

or

$$\theta_s = \frac{0.77}{2\pi}\frac{\lambda}{d_0} \simeq 0.12\frac{\lambda}{d_0} . \tag{13.91}$$

In the case of Kolmogorov turbulence, which is discussed later in this section, $\beta = 5/6$. Numerical integration of Eq. (13.88) yields

$$\theta_s \simeq 2.75 a^{6/5}\lambda^{-1/5} \simeq 0.30\frac{\lambda}{d_0} . \tag{13.92}$$

Plots of $\overline{w}_a(\theta)$ for various power-law models of phase fluctuations are shown in Fig. 13.11b.

Now consider the case of an interferometer operating in the domain of baselines greater than d_m, where σ_ϕ is a constant equal to σ_m. This case is most applicable to VLBI arrays or to large connected-element arrays. If the timescale of the fluctuation is short with respect to the measurement time, then, on average, all the visibility measurements are reduced by a constant factor $e^{-\sigma_m^2/2}$. Thus, this type of atmospheric fluctuation does not reduce the resolution. However, on average, the measured flux density is reduced from the true value by the factor $e^{-\sigma_m^2/2}$. If the timescale of the fluctuations is long with respect to the measurement time, then each visibility measurement suffers a phase error $e^{j\phi}$. Assume that K visibility measurements are made of a point source of flux density S. The image of the source, considering only one dimension for simplicity, is

$$\overline{w}_a(\theta) = \frac{S}{K} \sum_{i=1}^{K} e^{j\phi_i} e^{j2\pi u_i \theta} \; . \tag{13.93}$$

The expectation of $\overline{w}_a(\theta)$ at $\theta = 0$ is

$$\langle \overline{w}_a(0) \rangle = S e^{-\sigma_m^2/2} \; . \tag{13.94}$$

The measured flux density is less than S. (Note: $\langle \overline{w}_a(0) \rangle / S$ is sometimes called the coherence factor of the interferometer.) The missing flux density is scattered around the map. This is immediately evident from Parseval's theorem:

$$\sum_i \left| \overline{w}_a(\theta_i) \right|^2 = \frac{1}{K} \sum_i \left| \mathcal{V}(u_i) \right|^2 = S^2 \; . \tag{13.95}$$

Thus, the total flux density could be obtained by integrating the square of the image-plane response. The rms deviation in the flux density, measured at the peak response for a source at $\theta = 0$, is $\sqrt{\langle \overline{w}_a^2(\theta) \rangle - \langle \overline{w}_a(\theta) \rangle^2}$, which we call σ_S. This quantity can be calculated from Eq. (13.93) and is given by

$$\sigma_S = \frac{S}{\sqrt{K}} \sqrt{1 - e^{-\sigma_m^2}} \; , \tag{13.96}$$

which reduces to $\sigma_S \simeq S\sigma_m / \sqrt{K}$ when $\sigma_m \ll 1$.

13.1.7 Kolmogorov Turbulence

The theory of propagation through a turbulent neutral atmosphere has been treated in detail in the seminal publications of Tatarski (1961, 1971). This theory has been developed and applied extensively to problems of optical seeing [e.g., Roddier (1981), Woolf (1982), Coulman (1985)] and to infrared interferometry (Sutton et al. 1982). We confine the discussion here to a few central ideas concerning the structure

function of phase and indicate how it is related to other functions that are used to characterize atmospheric turbulence.

When the Reynolds number (a dimensionless parameter that involves the viscosity, a characteristic scale size, and the velocity of a flow) exceeds a critical value, the flow becomes turbulent. In the atmosphere, the Reynolds number is nearly always high enough that turbulence is fully developed. In the Kolmogorov model for turbulence, the kinetic energy associated with large-scale turbulent motions is transferred to smaller and smaller scale sizes of turbulence until it is finally dissipated into heat by viscous friction. If the turbulence is fully developed and isotropic, then the two-dimensional power spectrum of the phase fluctuations (or the refractive index) varies as $q_s^{-11/3}$, where q_s (cycles per meter) is the spatial frequency (q_s, the conjugate variable of d, is analogous to q, the conjugate variable of θ). The structure function for the refractive index $D_n(d)$ is defined in a fashion similar to the structure function of phase in Eq. (13.76); that is, $D_n(d)$ is the mean-squared deviation of the difference in the refractive index at two points a distance d apart, or $D_n(d) = \langle [n(x) - n(x-d)]^2 \rangle$. Note that only the scalar separation d is important for isotropic turbulence. For the conditions stated above, D_n can be shown to be given by the equation

$$D_n(d) = C_n^2 d^{2/3} , \qquad d_{\text{in}} \ll d \ll d_{\text{out}} , \tag{13.97}$$

where d_{in} and d_{out} are called the inner and outer scales of turbulence, which may be less than a centimeter and a few kilometers, respectively. The parameter C_n^2 characterizes the strength of the turbulence. Note that water vapor, which is the dominant cause of fluctuation in the index of refraction, is poorly mixed in the troposphere and therefore may be only an approximate tracer of the mechanical turbulence.

The details of the derivation structure function of phase from the structure function of the index of refraction given in Eq. (13.97) are given in Appendix 13.2. The result is that $D_\phi(d)$ for a uniform layer of turbulence of thickness L has several important power-law segments:

$$\begin{aligned} D_\phi(d) &\sim d^{5/3} , & d_r < d < d_2 , \\ &\sim d^{2/3} , & d_2 < d < d_{\text{out}} , \\ &\sim d^0 , & d_{\text{out}} < d . \end{aligned} \tag{13.98}$$

d_r is the limit where diffractive effects become important. $d_r \simeq \sqrt{L\lambda}$, so for an atmospheric layer of $L = 2$ km, d_r varies from 1.4 to 40 m for λ ranging from 1 mm to 1 m. This inner turbulence scale d_{in} is considerably smaller and of interest only at optical wavelengths. d_2 marks the transition from 3-D turbulence and 2-D turbulence caused by the thickness of the layer. Stotskii (1973 and 1976) was the first to recognize the importance of this break for radio arrays (see also Dravskikh and Finkelstein 1979). d_{out} is the distance beyond which the fluctuations

are uncorrelated, as described in Sect. 13.1.6. $d_{\rm out}$ is nominally the scale size of clouds, a few kilometers. However, some correlation remains out to the scale size of weather systems and beyond.

The structure function is formally an ensemble average. For practical purposes, the turbulent eddies are assumed to remain fixed as the atmospheric layer moves across an array. This is the frozen-screen hypothesis, sometimes attributed to Taylor (1938). Practically, the rms fluctuations in phase increase with time up to the cross time $t_c = d/v_s$, where v_s is the wind speed parallel to the baseline direction corresponding to d. t_c is called the corner time, beyond which the rms fluctuations flatten out and $D_\phi(d)$ can be estimated. Atmospheric fluctuations on scales larger than d cover both receiving elements and do not contribute to the structure function. An example of the structure function as a function of time measured at the ALMA site by the 300-m satellite site-testing interferometer is shown in Fig. 13.12. $t_c \sim 20$ s, implying a wind speed of about 15 m s^{-1}.

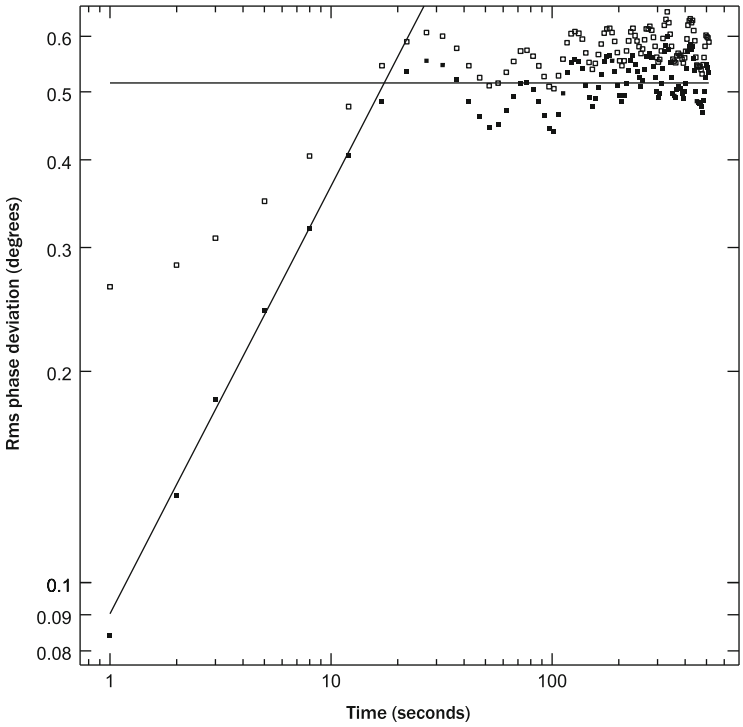

Fig. 13.12 The rms phase deviation at the ALMA site, measured with a satellite site-testing interferometer with a 300-m baseline at 11 GHz. The open symbols represent actual measurements; the solid symbols have the instrument noise removed. The line through the data has a slope of 0.6, as approximately expected by Kolmogorov theory [see Eq. (13.108)]. The break in the slope of the data occurs at the instrument crossing time, t_c. An estimate of the ensemble average of the structure function is reached for $t > t_c$. From Holdaway et al. (1995a).

We continue this section with a discussion of the primary case of 3-D turbulence in which $D_\phi \sim d^{5/3}$ and then generalize the results for other power-law indices. As derived in Appendix 13.2, for a uniform turbulence layer,

$$D_\phi(d) = 2.91\left(\frac{2\pi}{\lambda}\right)^2 C_n^2 L\, d^{5/3} , \tag{13.99}$$

which is valid in the range $\sqrt{L\lambda} \ll d \ll L$. The lower limit on d is equivalent to the requirement that diffraction effects be negligible. Note that the factor 2.91 is a dimensionless constant, and C_n^2 has units of length$^{-2/3}$. This factor appears in calculations based on D_n as defined in Eq. (13.97). (It is sometimes absorbed into C_n^2.)

We can generalize Eq. (13.99) for a stratified turbulent layer. The structure function of phase for an atmosphere in which C_n^2 varies with height from the surface to an overall height L is given by

$$D_\phi(d) = 2.91\left(\frac{2\pi}{\lambda}\right)^2 d^{5/3} \int_0^L C_n^2(h)\, dh . \tag{13.100}$$

The rms phase deviation is the square root of the phase structure function, or, when C_n^2 is a constant,

$$\sigma_\phi = 1.71\left(\frac{2\pi}{\lambda}\right)\sqrt{C_n^2 L}\, d^{5/6} . \tag{13.101}$$

The baseline length for which $\sigma_\phi = 1$ rad is defined as d_0 and is given by

$$d_0 = 0.058\lambda^{6/5}(C_n^2 L)^{-3/5} . \tag{13.102}$$

Another scale length that is proportional to d_0 is the Fried length, d_f (Fried 1966). This scale is particularly useful for discussions of the effects of turbulence in telescopes with circular apertures and is widely used in the optical literature. The structure function of phase can be written as $D_\phi = 6.88(d/d_f)^{5/3}$, where the factor 6.88 is an approximation of $2[(24/5)\Gamma(6/5)]^{5/6}$ (Fried 1967). Hence, from Eqs. (13.99) and (13.102), $d_f = 3.18 d_0$. The Fried length is defined such that the effective collecting area of a large circular aperture with uniform illumination in the presence of Kolmogorov turbulence is $\pi d_f^2/4$. Hence, for an aperture of diameter small with respect to d_f, the resolution is dominated by diffraction at the aperture. With an aperture large with respect to d_f, the resolution is set by the turbulence and is approximately λ/d_f. The exact resolution in this latter case can be derived from Eq. (13.92), with the result $\theta_s = 0.97\lambda/d_f$. In addition, the rms phase error over an aperture of diameter d_f is 1.01 rad. The reason that d_f is larger than d_0 is related to the downweighting of long baselines in two-dimensional apertures [see Eq. (15.13) and related discussion]. For an aperture of diameter d_f, the ratio of the collecting

area to the geometric area, which is called the Strehl ratio in the optical literature, is equal to 0.45 (Fried 1965).

Equation (13.102) shows that d_0 is proportional to $\lambda^{6/5}$, and thus the angular resolution or seeing limit ($\sim \lambda/d_0$) is proportional to $\lambda^{-1/5}$ [see Fig. 13.11 and Eq. (13.92)]. This relationship may hold over broad wavelength ranges when C_n^2 is constant. In the optical range, C_n^2 is related to temperature fluctuations, whereas in the radio range, C_n^2 is dominated by turbulence in the water vapor. It is an interesting coincidence that the seeing angle is about $1''$ at both optical and radio wavelengths, for good sites. The important difference is the timescale of fluctuations, $\tau_{\rm cr}$. If the critical level of fluctuation is 1 radian, then $\tau_{\rm cr} \simeq d_0/v_s$, where v_s is the velocity component of the screen parallel to the baseline. Any adaptive optics compensation must operate on a timescale short with respect to $\tau_{\rm cr}$. From Eq. (13.92), $\tau_{\rm cr}$ can be expressed as

$$\tau_{\rm cr} \simeq 0.3 \frac{\lambda}{\theta_s v_s} \,. \tag{13.103}$$

For $v_s = 10$ m s^{-1} and $\theta_s = 1''$, $\tau_{\rm cr} = 3$ ms at 0.5 μm wavelength and 60 s at 1 cm wavelength.

The two-dimensional power spectrum of phase, $\mathcal{S}_2(q_x, q_y)$, is the Fourier transform of the two-dimensional autocorrelation function of phase, $R_\phi(d_x, d_y)$. If R_ϕ is a function only of d, where $d^2 = d_x^2 + d_y^2$, then $\mathcal{S}_2$ is a function of q_s, where $q_s^2 = q_x^2 + q_y^2$, and $\mathcal{S}_2(q_s)$ and $R_\phi(d)$ form a Hankel transform pair. Since $D_\phi(d) = 2[R_\phi(0) - R_\phi(d)]$, we can write

$$D_\phi(d) = 4\pi \int_0^\infty [1 - J_0(2\pi q_s d)]\, \mathcal{S}_2(q_s) q_s \, dq_s \,, \tag{13.104}$$

where J_0 is the Bessel function of order zero. When $D_\phi(d)$ is given by Eq. (13.100), $\mathcal{S}_2(q_s)$ is

$$\mathcal{S}_2(q_s) = 0.0097 \left(\frac{2\pi}{\lambda}\right)^2 C_n^2 L q_s^{-11/3} \,. \tag{13.105}$$

It is often useful to study temporal variations caused by atmospheric turbulence. In order to relate the temporal and spatial variations, we invoke the frozen-screen hypothesis. The one-dimensional temporal spectrum of the phase fluctuations $\mathcal{S}'_\phi(f)$ (the two-sided spectrum) can be calculated from $\mathcal{S}_2(q_s)$ by

$$\mathcal{S}'_\phi(f) = \frac{1}{v_s} \int_{-\infty}^{\infty} \mathcal{S}_2 \left(q_x = \frac{f}{v_s}, q_y\right) dq_y \,, \tag{13.106}$$

where v_s is in meters per second. Substitution of Eq. (13.105) into Eq. (13.106) yields

$$\mathcal{S}'_\phi(f) = 0.016 \left(\frac{2\pi}{\lambda}\right)^2 C_n^2 L v_s^{5/3} f^{-8/3} \ (\text{rad}^2\ \text{Hz}^{-1}) \ . \tag{13.107}$$

Examples of the temporal spectra of water vapor fluctuations can be found in Hogg et al. (1981) and Masson (1994a) (see Fig. 13.17). The temporal structure function $D_\tau(\tau) = \langle[\phi(t) - \phi(t-\tau)]^2\rangle$ is related to the spatial structure function by $D_\tau(\tau) = D_\phi(d = v_s\tau)$. Hence, for Kolmogorov turbulence, we obtain from Eq. (13.99)

$$D_\tau(\tau) = 2.91 \left(\frac{2\pi}{\lambda}\right)^2 C_n^2 L v_s^{5/3} \tau^{5/3} \ . \tag{13.108}$$

$D_\tau(\tau)$ and $\mathcal{S}'_\phi(f)$ are related by a transformation similar to Eq. (13.104). The use of temporal structure functions to estimate the effects of fluctuations on interferometers is discussed by Treuhaft and Lanyi (1987) and Lay (1997a).

The Allan variance $\sigma_y^2(\tau)$, or fractional frequency stability for time interval τ, associated with $\mathcal{S}'_\phi(f)$ has been defined in Sect. 9.5.1. It can be calculated by substituting Eq. (9.119) into Eq. (9.131), which gives

$$\sigma_y^2(\tau) = \left(\frac{2}{\pi \nu_0 \tau}\right)^2 \int_0^\infty \mathcal{S}'_\phi(f) \sin^4(\pi\tau f)\, df \ . \tag{13.109}$$

By substituting Eq. (13.107) into Eq. (13.109), and noting that

$$\int_0^\infty [\sin^4(\pi x)]/x^{8/3}\, dx = 4.61 \ ,$$

we obtain

$$\sigma_y^2(\tau) = 1.3 \times 10^{-17} C_n^2 L v_s^{5/3} \tau^{-1/3} \ . \tag{13.110}$$

Armstrong and Sramek (1982) give general expressions for the relations among $\mathcal{S}_2, \mathcal{S}'_\phi, D_\phi$, and σ_y for an arbitrary power-law index. If $\mathcal{S}_2 \propto q^{-\alpha}$, then $D_\phi(d) \propto d^{\alpha-2}$, $\mathcal{S}'_\phi \propto f^{1-\alpha}$, and $\sigma_y^2 \propto \tau^{\alpha-4}$. These relations are summarized in Table 13.2.

The actual behavior of the atmosphere is more complex than described above, but the theory developed provides a general guide. An example of a structure function of phase from the VLA is shown in Fig. 13.13 (see also Fig. 13.22 for a similar plot for ALMA). It clearly shows the three power-law regions, with power-law exponents close to their expected values. The effects of phase noise on VLBI observations are discussed by Rogers and Moran (1981) and Rogers et al. (1984). The plot of Allan variance by Rogers and Moran is shown in Fig. 9.17.

Table 13.2 Power law relations for turbulence

Quantity			Exponent	
			3-D turbulence ($\alpha = 11/3$)	2-D turbulence ($\alpha = 8/3$)
2-D, 3-D power spectrum	$\mathcal{S}_2(q_s), \mathcal{S}(q_s)$	$-\alpha$	$-11/3$	$-8/3$
Structure function	$D_\phi(d)$	$\alpha - 2$	5/3	2/3
Temporal phase spectrum	$\mathcal{S}'_\phi(f)$	$1 - \alpha$	$-8/3$	$-5/3$
Allan variance	$\sigma_y^2(\tau)$	$\alpha - 4$	$-1/3$	$-4/3$
Temporal structure function	$D_\tau(\tau)$	$\alpha - 2$	5/3	2/3

Adapted from Wright (1996, p. 526).

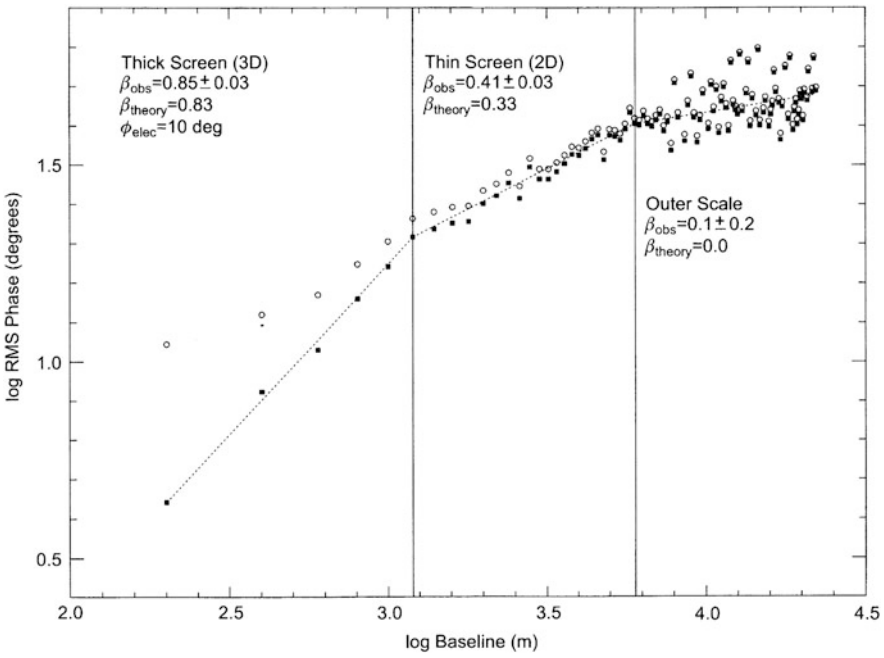

Fig. 13.13 The root phase structure function (rms phase) from observations with the VLA at 22 GHz. The open circles show the rms phase variation vs. baseline length measured on the source 0748+240 over a period of 90 min. The filled squares show the data after removal of a constant receiver-induced noise component of rms amplitude 10°. The three regimes of the phase structure function are indicated by vertical lines (at 1.2 and 6 km). Note that $\beta = \alpha/2$. From Carilli and Holdaway (1999). © 1999 by the American Geophys. Union.

13.1.8 Anomalous Refraction

The beamwidths of many millimeter radio telescopes are sufficiently small that the effect of atmospheric phase fluctuations can be detected. This effect was first noticed with the 30-m-diameter millimeter-wavelength telescope on Pico de Veleta, where the apparent positions of unresolved sources were observed to wander by about 5″ on timescales of a few seconds under certain meteorological conditions [see, e.g., Altenhoff et al. (1987), Downes and Altenhoff (1990), and Coulman (1991)]. This motion is due to the flow of the turbulent layer of water vapor across the telescope aperture, which is distinct from the refraction caused by the quasi-static atmosphere, and hence the term "anomalous refraction." This effect can be understood by a simple application of the theory developed in Sect. 13.1.7. The magnitude of the refraction is dominated by the turbulent cells of size equal to the diameter of the antenna. These cells can be thought of as refractive wedges moving across the aperture of the antenna. The rms value of the differential phase shift of such a wedge is equal to the square root of the structure function evaluated at the separation distance equal to the diameter of the antenna, $\sqrt{D_\phi(d)}$. Hence, the rms value of the anomalous refraction for an observation at zenith is given by

$$\epsilon = \frac{\sqrt{2D_\phi(d)}}{d} \,, \tag{13.111}$$

where the structure function is in units of length and the factor of two accounts for motion in both azimuth and elevation. Note that fluctuations on larger scales than d are unimportant as long as the power-law exponent on the structure function is less than two, as is usually the case. In the 3-D turbulence case, ϵ will vary as $\sqrt{\sec z}$. If we express the rms phase fluctuations as $\sigma = \sigma_0(d/100m)^{5/6}$ (see Table 13.4 for values of σ_0), then the ratio of the anomalous refraction angle to the beamwidth, $\theta_b \sim 1.2\lambda/d$, is

$$\epsilon/\theta_b \simeq 1.2\frac{\sigma_0}{\lambda}\left(\frac{d}{100m}\right)^{5/6} \,. \tag{13.112}$$

For example, the range of seasonal median values for σ_0 for the ALMA site is 0.045–0.17 mm. Since the diameter of the ALMA antennas is 12 m, the range of ϵ is 0.2–0.6″ from Eq. (13.111), which is independent of wavelength. The timescale of this effect is d/v_s, where v_s is the wind speed. At a wavelength of 1 mm, the beamwidth is about 20″, so the ratio ϵ/θ_b has the range of 1% to 3%. There is no effect on the amplitude of the incident electric field because the phase fluctuations arise in a layer close to ground. However, the fractional changes in antenna gain at the half-beamwidth point would range from 1.5% to 5%, which could have an effect on the quality of mosaic images derived from array observations under some conditions. For further details, see Holdaway and Woody (1998). Methods of real-time correction of anomalous refraction have been proposed by Lamb and Woody (1998).

13.2 Site Evaluation and Data Calibration

13.2.1 Opacity Measurements

At millimeter and submillimeter wavelengths, absorption and path length fluctuations in the atmosphere limit performance in synthesis imaging. This section is concerned with monitoring of atmospheric parameters for optimum choice of sites and with methods of calibrating the atmosphere to reduce phase errors. This subject has received much attention as a result of the development of major instruments at millimeter and submillimeter wavelengths.

For given atmospheric parameters, the zenith opacity (optical depth) τ_0 can be calculated as a function of frequency using the propagation models of Liebe (1989), Pardo et al. (2001a), or Paine (2016). Figure 13.14 shows curves of transmission, $\exp(-\tau_0)$, for 4 mm of precipitable water at an elevation of 2124 m and 1 mm at 5000 m, corresponding to the VLA and ALMA sites, respectively. For the purpose of choosing a suitable observatory site, detailed monitoring of the atmosphere covering both diurnal and annual variation is necessary. We assume that the zenith opacity has the form

$$\tau_\nu = A_\nu + B_\nu w \,, \tag{13.113}$$

where A_ν and B_ν are empirical constants that depend on frequency, site elevation, and meteorological conditions. Selected measurements of these constants are given in Table 13.3.

The opacity can be monitored by measuring the total noise power received in a small antenna as a function of zenith angle (i.e., the tipping-scan method described in Sect. 13.1.3). A commonly used frequency for opacity monitoring is 225 GHz, which lies within the 200–310 GHz atmospheric window (see Figs. 13.7 and 13.14) in the vicinity of the important CO 2–1 rotational transition at 230 GHz.

A typical site-test radiometer designed for opacity measurements uses a small parabolic primary reflector with a beamwidth of $\sim 3°$ at 225 MHz. A wheel with blades that act as plane reflectors is inserted at the beam waist between the primary and secondary reflectors and sequentially directs the input of the receiver to the output of the antenna, a reference load at 45 °C, and a calibration load at 65 °C. The amplified signals go to a power-linear detector and then to a synchronous detector that produces voltages proportional to the difference between the antenna and the 45 °C load, which is the required output, and the difference between the 45 ° and 65 °C loads, which provides a calibration. Measurements of the antenna temperature are made at a range of different zenith angles. When connected to the antenna, the measured noise temperature of such a system, $T_{\rm meas}$, consists of three components:

$$T_{\rm meas} = T_{\rm const} + T_{\rm at}(1 - e^{-\tau_0 \sec z}) + T_{\rm cmb} e^{-\tau_0 \sec z} \,. \tag{13.114}$$

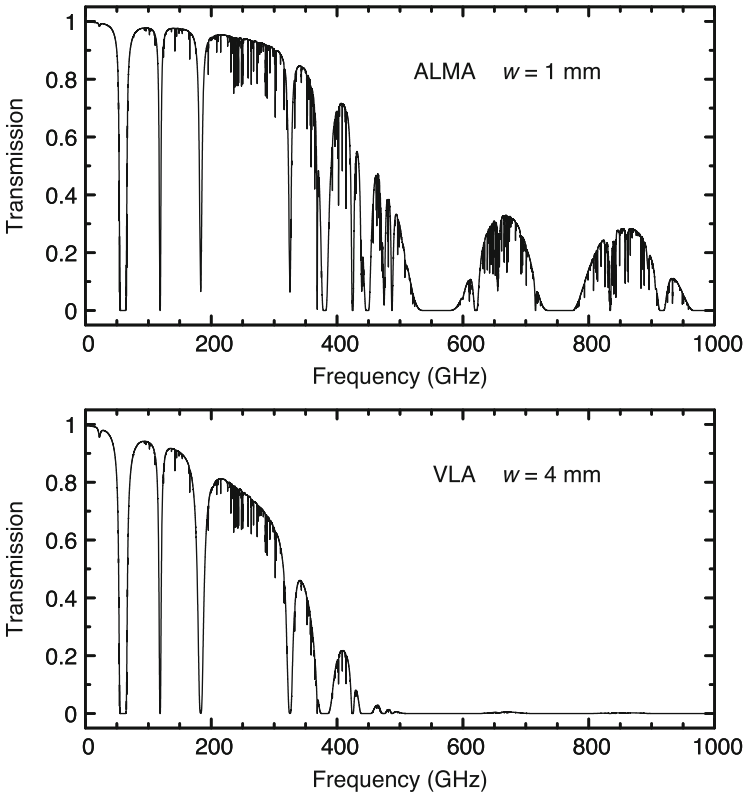

Fig. 13.14 (**top**) The zenith atmospheric transmission (equal to e^{τ}) at the ALMA site (5000 m, with 1 mm of precipitable water vapor). There are additional windows with transmissions of about 0.3% near 1100, 1300, and 1500 GHz. There are no additional windows with higher transmission up to 7500 GHz (40 μm). (**bottom**) The zenith transmission at the VLA site (2124 m, with 4 mm of precipitable water). Note that the transmission depends on the altitude because of the pressure broadening of the absorption lines. Because of this effect, for a fixed value of w, the transmission at any frequency in an atmospheric window will be lower for lower altitude sites. The many narrow absorption features (line widths of $\sim$ 100 MHz) are caused by stratospheric ozone lines [for a catalog of these lines, see Lichtenstein and Gallagher (1971)]. The effects of these lines in astronomical observations can be removed by careful bandpass calibration. These transmission plots were calculated with the *am* code (Paine 2016) with profiles for mean midlatitude atmospheric conditions.

Here $T_{\rm const}$ represents the sum of noise components that remain constant as the antenna elevation is varied, that is, the receiver noise, thermal noise resulting from losses between the antenna and the receiver input, any offset in the radiometer detector, and so on. The second term in Eq. (13.114) represents the component of noise from the atmosphere: $T_{\rm at}$ is the temperature of the atmosphere, and z is the zenith angle. $T_{\rm cmb} \simeq 2.7$ K represents the cosmic microwave background radiation. It will be assumed that $T_{\rm at}$ and $T_{\rm cmb}$ represent brightness temperatures that are related

Table 13.3 Zenith opacity as a function of column height of water vapor

ν (GHz)	Location[a]	Altitude (m)	A_ν (nepers)	B_ν (nepers mm^{-1})	Method[b]	Ref.[c]
15	Sea level	0	0.013	0.002	1	1
22.2	Sea level	0	0.026	0.02	1	1
35	Sea level	0	0.039	0.006	1	1
90	Sea level	0	0.039	0.018	1	1
225	South Pole	2835	0.030	0.069	2	2
225	Mauna Kea	4070	0.01	0.04	2	3
225	Chajnantor	5000	0.006	0.033	2	4
225	Chajnantor	5000	0.007	0.041	2	5
493	South Pole	2835	0.33	1.49	2	6

[a]Locations: South Pole = Amundsen–Scott station; Mauna Kea = site of submillimeter telescopes on Mauna Kea; Chajnantor = Llano de Chajnantor, Atacama Desert, Chile.
[b]Methods: (1) opacity derived from radiosonde data, water vapor estimated from surface humidity and scale height of 2 km; (2) opacity derived from tipping radiometer, water vapor column height derived from radiosonde data.
[c]References: (1) Waters (1976); (2) Chamberlin and Bally (1995); (3) Masson (1994a); (4) Holdaway et al. (1996); (5) Delgado et al. (1998); (6) Chamberlin et al. (1997).

to the physical temperatures by the Planck or Callen and Welton formulas (see Sect. 7.1.2). If $T_{\rm at}$ is known, it is straightforward to determine τ_0 from $T_{\rm meas}$ as a function of z. The temperature of the atmosphere is assumed to fall off from the ambient temperature at the Earth's surface $T_{\rm amb}$, with a lapse rate l considered to be constant with height. Thus, at height h, the temperature is $T_{\rm amb} - lh$. We require the mean temperature weighted in proportion to the density of water vapor, which is exponentially distributed with scale height h_0:

$$T_{\rm at} = T_{\rm amb} - \frac{l\int_0^\infty he^{h/h_0}\,dh}{\int_0^\infty e^{h/h_0}\,dh} = T_{\rm amb} - lh_0\ . \tag{13.115}$$

The lapse rate resulting from adiabatic expansion of rising air, 9.8 K km^{-1}, can be used as an approximate value, but as indicated earlier, a typical measured value is $\sim$ 6.5 K km^{-1}. The scale height of water vapor is approximately 2 km. Thus, $T_{\rm at}$ is typically less than $T_{\rm amb}$ by $\sim$ 13–20 K.

Figure 13.15 displays examples of data taken on Mauna Kea, which show the diurnal and seasonal effects at this site. The cumulative distribution of zenith opacity at 225 and 850 GHz as measured at Cerro Chajnantor, Llano de Chajnantor in Chile; Mauna Kea; and the South Pole are shown in Fig. 13.16. Measurements of mean opacity provide a basis for calculating the loss in sensitivity due to absorption of the signal and the addition of noise from the atmosphere [see Eq. (13.50)]. The opacity varies both diurnally and annually, so measurements at hourly intervals

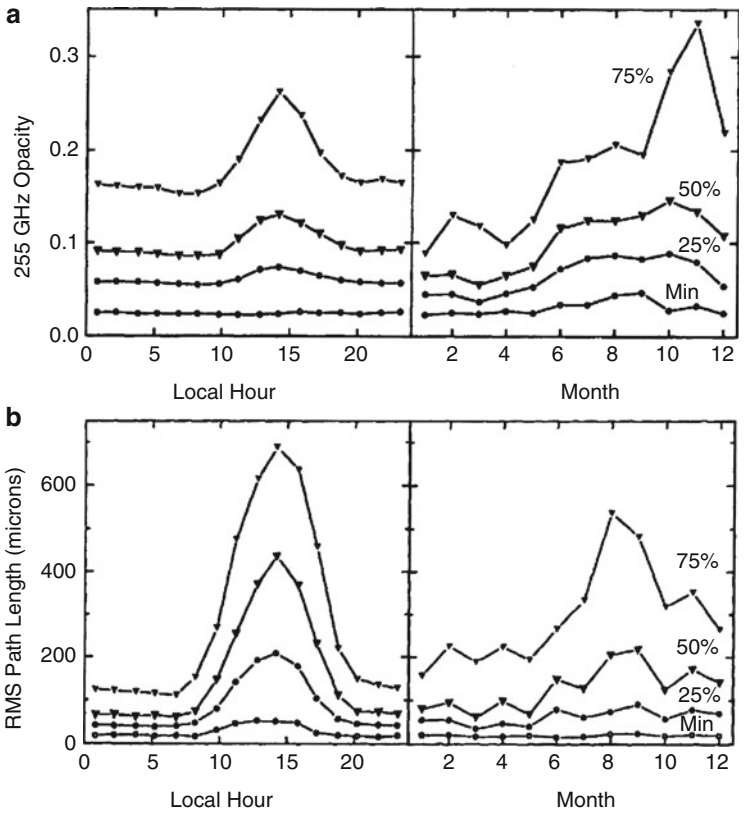

Fig. 13.15 (**a**) Diurnal and seasonal zenith opacity at 225 GHz measured at the CSO site on Mauna Kea (4070-m elevation) for a three-year period (August 1989–July 1992) computed from 14,900 measurements. The minimum value and the 25th, 50th, and 75th percentiles are shown. The increase in opacity during the day is caused by an inversion layer that rises above the mountain in the afternoons. (**b**) Diurnal and seasonal variation of the rms path length on Mauna Kea on a 100-m baseline, determined from observations of a geostationary satellite at 11 GHz. From Masson (1994a), courtesy of and © the Astronomical Society of the Pacific.

over a year or more are required for reliable comparison of different sites. Long-term variability due to climatic effects (e.g., El Niño) can be significant. Table 13.3 shows the effect of site altitude on opacity. Comparison of the measurements of A_ν and B_ν show that both parameters decrease with altitude because of the effects of pressure broadening. Comparisons of opacities at various frequencies can be made with broadband Fourier transform spectrometers (Hills et al. 1978; Matsushita et al. 1999; Paine et al. 2000; Pardo et al. 2001b).

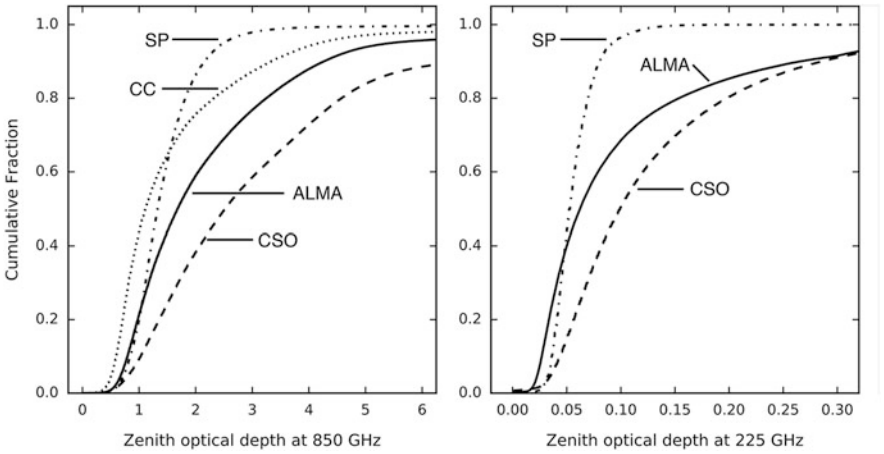

Fig. 13.16 Cumulative distributions of the zenith optical depth at 850 GHz (**left panel**) and at 225 GHz (**right panel**) at Cerro Chajnantor, Chile (5612-m elevation); the ALMA site on Llano de Chajnantor, Chile (5060-m elevation); the CSO on Mauna Kea, Hawaii (4100-m elevation); and the South Pole (2835-m elevation) for the periods April 1995–April 1999, Jan. 1997–July 1999, and Jan. 1992–Dec. 1992, respectively. Note that the median opacity at 225 GHz at the VLBA site on Mauna Kea (3720-m elevation) for the same time interval at the CSO site was 0.13. The median opacity for the VLA site (2124-m elevation) for the period 1990–1998 was 0.3 (Butler 1998). Conditions at lower elevation sites are correspondingly worse. For example, at a sea-level site in Cambridge, MA, the 225-GHz opacity, inferred from measurements at 115 GHz, was 0.5 for the six-month winter observing seasons spanning 1994–1997. Conditions on Dome C, Antarctica (3260-m elevation), are significantly better than at the South Pole (Calisse et al. 2004), and Ridge A on the Antarctic high plateau (4050-m elevation) may have the lowest water vapor on the planet (Sims et al. 2012). Adapted from Radford and Peterson (2016).

13.2.2 Site Testing by Direct Measurement of Phase Stability

Interferometer observations provide a direct method of determining atmospheric phase fluctuations. Signals from a geostationary satellite are usually used, since strong signals can be obtained using small, nontracking antennas. This technique, called satellite-tracking interferometry (STI), was developed by Ishiguro et al. (1990); Masson (1994a); and Radford et al. (1996). It was used in site testing for the SAO Submillimeter Array on Mauna Kea, Hawaii, Atacama Large Millimeter/submillimeter Array at Llano de Chajnantor, and potential SKA sites. Several suitable geostationary-orbit satellites operate in bands allocated to the fixed and broadcasting services near 11 GHz. Two commercial satellite TV antennas of diameter 1.8 m provide signal-to-noise ratios close to 60 dB. For measurements of atmospheric phase, baselines of 100–300 m have been used. The residual motion of the satellite, as well as any temperature variations, can cause unwanted phase drifts. These are generally slow compared with the atmospheric effects and can be removed by subtracting a mean and slope from the output data. The variance of the fluctuations resulting from the system noise can also be determined and subtracted

from the variance of the measured phases. The test interferometer provides a measure of the structure function of phase $D_\phi(d)$ for one value of projected baseline d (see Fig. 13.15b).

It is sometimes useful to compare the quality of sites based on STI measurements made with different baselines and zenith angles. For baselines in the vicinity of 100 m (see also Fig. A13.4), a reasonable scaling is

$$\sigma_\phi \sim \sigma_0 d^{5/6} \sqrt{\sec z}\,. \tag{13.116}$$

For longer baselines, other power laws will be more appropriate.

With the frozen-screen approximation, the power-law exponent can be determined from the power spectrum of the fluctuations. An example is shown in Fig. 13.17 (see also Bolton et al. 2011). Thus, in extrapolating $D_\phi(d)$ from a single-spacing measurement, one does not have to depend on the theoretical values of the exponent of d but can use the measurements of $D_\phi(\tau)$ to determine the range and variation [see Eq. (13.108) and Table 13.2]. For the example shown in Fig. 13.17, the power-law slope for frequencies above 0.01 Hz is 2.5, slightly below the value of 8/3 or 2.67 predicted for Kolmogorov turbulence. The spectrum flattens at frequencies below 0.01 Hz because of the filtering effect of the interferometer. Fluctuations larger than the baseline, 100 m in this case, cause little phase effect. For the corner frequency $f_c = v_s/d$, the wind speed along the baseline direction can be inferred to be about 1 m s^{-1}.

Table 13.4 shows a compilation of the measurements of the structure function referred to a baseline of 100 m. The range of values reported for a fiducial baseline

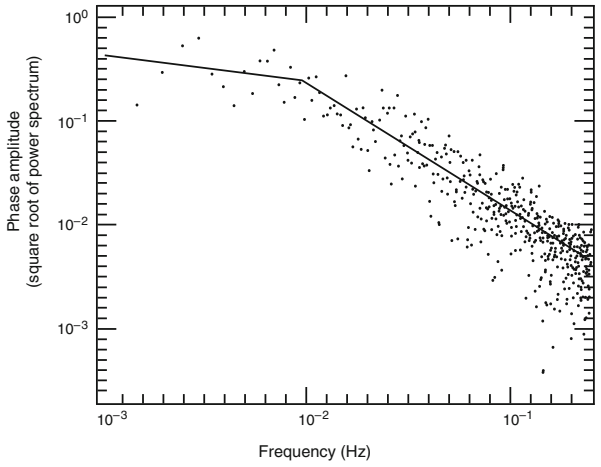

Fig. 13.17 The square root of the temporal power spectrum [i.e., Eq. (13.107)] measured on a 100-m baseline on Mauna Kea (CSO site). The tropospheric wind speed along the baseline can be computed from the break in the spectrum. From Masson (1994a), courtesy of and © the Astronomical Society of the Pacific.

Table 13.4 Site phase stability characteristics

Location	ID	Altitude (m)	Baseline (m)	Frequency (GHz)	Type[a]	No. of days	Date of data	σ[b] (mm)	β[c]	Ref.[d]
Cambridge, UK		17	1000	5	A	50	Jan 1969–Sep 1969	0.12–0.5	0.6	1
Murchison, Australia	MRO	370	200	11.7	S	180	Jun 2011–Sep 2011	0.15–0.38	—	2
Green Bank, USA		840	2400	2.7	A	25	Mar 1965–Aug 1965	0.2–0.8	—	3
Goldstone (A), USA	DSN	952	190	12.5	S	700	Jan 2011–Dec 2012	0.12–0.31	0.7	4
Hat Creek, USA		1043	6–850	86	A	10	Nov 1993–Feb 1995	0.11–0.3	0.4–0.7	5
Goldstone (V), USA		1070	256	20.2	S	700	Jan 2011–Dec 2012	0.083–0.22	0.6	4
Karoo, South Africa	RSA	1081	200	11.7	S	180	Mar 2011–Oct 2011	0.12–0.25	—	6
Nobeyama, Japan		1350	50–500	22	A	2	Feb 1985–May 1985	0.15–0.4	0.8	7
VLA, USA		2124	50–8000	5.15	A	109	Dec 1983–Dec 1985	0.09–0.22	0.1–0.6	8
VLA, USA	VLA	2124	300	11.3	S	350	Sep 1998–Aug 1999	0.065–0.26	—	9
Plateau de Bure, France	PdB	2552	24–290	86	A	200	Feb 1990–Aug 1990	0.10–0.6	0.7	10
Mauna Kea, USA		4070	33–260	12	S	60	Nov 2011–Dec 2011	0.095	0.6	11
Mauna Kea, USA	SMA	4070	100	11.7	S	600	Dec 1990–Sep 1992	0.065–0.17	0.75	12
Pampa la Bola, Chile	PlaB	4800	300	11.7	S	1000	Jul 1996–Mar 1999	0.056–0.22	—	13
ALMA, Chile	ALMA	5000	300	11.7	S	1000	Jul 1996–Mar 1999	0.045–0.17	—	13

[a]A = astronomical data; S = satellite-tracking interferometry (STI) data.

[b]The rms phase deviation range referred to a baseline of 100 m usually represents the span from the median condition at nighttime during winter to daytime during summer.

[c]Power-law exponent for baseline length dependence. For astronomical data, β is derived from rms phase vs. baseline. For satellite-tracking interferometry data, β is derived from temporal power spectrum. $\beta = 5/6$ or 0.833 for 3-D turbulence and $2/3$ or 0.667 for 2-D turbulence.

[d]References: (1) Hinder (1970), Hinder and Ryle (1971), Hinder (1972); (2) Millenaar (2011a); (3) Baars (1967); (4) Morabito et al. (2013); (5) Wright (1996), see also Wright and Welch (1990), Bieging et al. (1984); (6) Millenaar (2011b); (7) Kasuga et al. (1986), see also Ishiguro et al. (1990); (8) Sramek (1990), see also Sramek (1983), Carilli and Holdaway (1999), Armstrong and Sramek (1982); (9) Butler and Desai (1999); (10) Olmi and Downes (1992); (11) Kimberk et al. (2012); (12) Masson (1994a); (13) Butler et al. (2001).

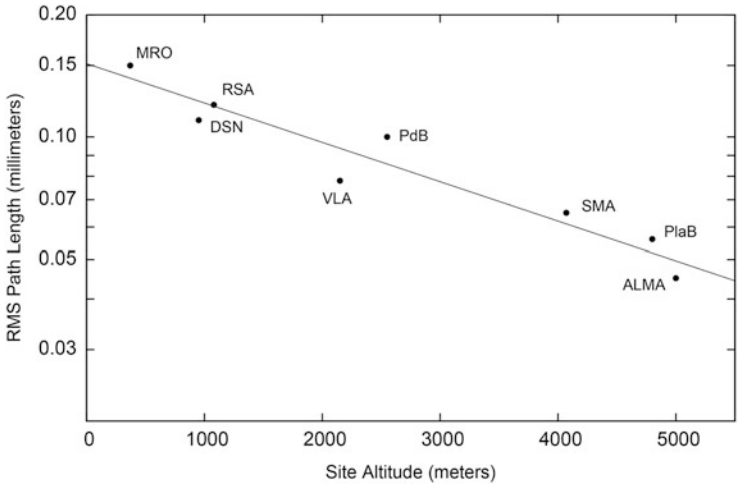

Fig. 13.18 Rms path length vs. site elevation referred to zenith and baseline of 100 m. Data taken in good weather conditions, i.e., winter nighttime (see Table 13.4 for station identifiers). Straight line is best-fit exponential with scale height of 2200 m and sea level intercept of 0.15.

of 100 m are meant to reflect the median conditions at night during the winter and daytime during the summer. The measurements were obtained either by satellite interferometry or astronomical measurements. A plot of the rms phase noise vs. site altitude for "best conditions" is presented in Fig. 13.18. The decrease of rms phase noise vs. altitude is evident. With the assumption that the turbulence, i.e., C_n^2, is proportional to water vapor density and that the water vapor is distributed exponentially with a scale height of h_0, we obtain from Eq. (13.100) the result

$$\sigma = \sigma_0 \, e^{-h/2h_0} \, . \tag{13.117}$$

(The factor of 2 arises from the fact that $\sigma_\phi = \sqrt{D_\phi}$. The line shown is a fit to this equation.) The value of h_0 is 2.2 km, close to the nominal scale height of 2 km, and $\sigma_0 = 0.05$ mm. Because the distillation of this information from disparate sources is difficult, the results are meant to show the importance of altitude rather than make small distinctions among observatories. Local conditions can also be important. See Masson (1994b) for further discussion.

A wide range of power-law indices has been observed (see Table 13.4). Much of the variation between 0.33 and 0.833 is due to the effects of thin scattering layers in the troposphere, which effectively moves or blurs the crossover from 2-D to 3-D turbulence (see Bolton et al. 2011). Beaupuits et al. (2005) explored this problem by pointing two 183-GHz water-vapor radiometers so that their beam intersected at an altitude of about 1500 m. By analyzing the delay between the radiometer signals, they identified a significant turbulent layer near 600 m.

The atmospheric phase noise, if left uncorrected, causes a coherence loss in an interferometer. For the model in Fig. 13.18, the baseline for which the coherence

factor C, equal to measured/true visibility defined in Eq. (13.80), can be derived from Eq. (13.117), giving

$$d_c = 100 \left[-\frac{\ln C}{2\pi^2} \left(\frac{\lambda}{\sigma_0} \right)^2 e^{h/h_0} \right]^{3/5} . \tag{13.118}$$

For example, with $\sigma_0 = 0.10\,\text{mm}$, $h_0 = 2200\,\text{m}$, $h = 5000\,\text{m}$, $\lambda = 1.3\,\text{mm}$, and $C = 0.9$, $d_c = 80\,\text{m}$.

13.3 Calibration via Atmospheric Emission

A practical method of estimating phase fluctuations is to measure the integrated water vapor in the direction of each antenna beam. This usually requires an auxiliary radiometer at each antenna to measure the sky brightness temperature. Water vapor is the main cause of opacity at radio frequencies (except for the oxygen bands at 50–70 and 118 GHz), even at frequencies well away from the centers of water vapor lines, as can be seen in Fig. 13.7. Away from the centers of spectral lines, the opacity is due to the far line wings of infrared transitions. There is also an important *continuum* component of the absorption caused by water vapor, which varies as ν^2 (Rosenkranz 1998). This component includes various quantum mechanical effects involving water molecules such as dimers (Chylek and Geldart 1997). It is usually necessary to model this component with an empirical coefficient. In addition, as described in Sect. 13.3.2, the water droplets in the form of clouds and fog, as well as ice crystals, contribute absorption that varies as ν^2. Hence, there are two distinct methods of calibration: those based on measurement of sky brightness in the bands between the lines (continuum) and those based on measurements near a spectral line (see Welch 1999). The sensitivities of the brightness temperature to the propagation delay are listed in Table 13.5 for selected frequencies.

13.3.1 Continuum Calibration

The method of measuring the continuum sky brightness at, say, 90 or 225 GHz has several advantages, as first described by Zivanovic et al. (1995). The same radiometers used for the astronomical measurements can be used for the sky brightness measurements. At 225 GHz, if phase calibration to an accuracy of a twentieth of a wavelength is required, then, from the sensitivity listed in Table 13.5, the brightness temperature accuracy required is 0.1 K. For a system temperature of 200 K, this accuracy requires a gain stability of 5×10^{-4}. Such stability usually requires special attention to the temperature stabilization of the receiver cryogenics. In addition, the gain scales must be accurately calibrated. Changes in ground pickup

Table 13.5 Brightness temperature sensitivity dT_b/dw (K/mm) for various frequencies at site elevations of 0 and 5 km for various values of precipitable water vapor[a]

		0-km elevation		5-km elevation	
ν (GHz)	Origin of opacity	$w = 0$ mm	15 mm	$w = 0$ mm	15 mm
22.2	Line center ($6_{16} - 5_{23}$)	1.9	1.7	2.8	2.8
90.0	Continuum	1.8	2.1[b]	1.2	1.2
183.3	Line center ($3_{13} - 2_{20}$)	294	0.0	527	51.4
185.0	Line wing ($3_{13} - 2_{20}$)	222	0.1	280	91.2
230.0	Continuum	15.9	7.3	11.4	9.8
690.0	Continuum	380	0.0	297	82.5

[a]Entries in this table were calculated with the *am* model (Paine 2016) for median midlatitude atmospheric profiles. Note that $w = 15$ and 0 mm are close to the measured values for midlatitudes for altitudes of 0 and 5 km, respectively. The effects of pressure broadening are clearly evident. For example, at $w = 0$, dT_b/dw is less at sea level than at 5 km for the 22.2- and 183.3-GHz spectral lines, while the opposite is true for the continuum bands. More detailed information about the brightness temperature sensitivity near the 183-GHz transition can be found in Fig. 13.21.
[b]More sensitive than for $w = 0$ because of the effect of H_2O line self-broadening.

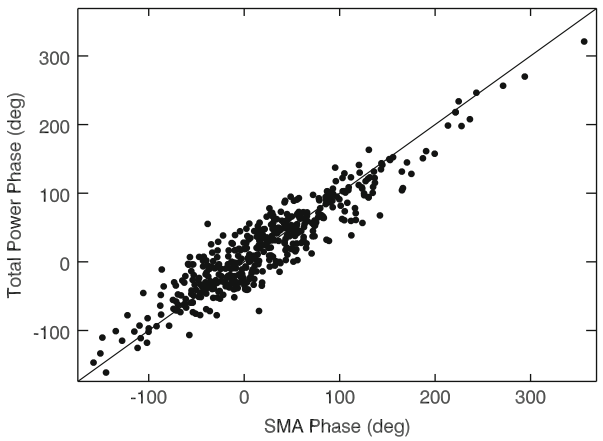

Fig. 13.19 Correlation between interferometric phase predicted by total power measurement at 230 GHz vs. interferometric phase. The data were taken over a period of 20 min on a 140-m baseline of the Submillimeter Array (SMA) on Mauna Kea. The total powers (i.e., antenna temperatures) at each antenna were used to estimate phase with a linear model having free parameters. The straight line shown has unity slope and zero intercept. The rms phase error is improved from 72 to 27°, corresponding to path length residuals of 260 to 98 μm, respectively. From Battat et al. (2004). © AAS. Reproduced with permission.

can be misinterpreted as sky brightness temperatures change. The presence of clouds defeats this method, because of the contribution of liquid water to the opacity. An example of viability of this type of calibration is shown in Fig. 13.19. The application of this method for the Plateau de Bure interferometer is described by Bremer (2002). For further discussion, see Matsushita et al. (2002).

13.3.2 22-GHz Water-Vapor Radiometry

The idea of determining the vertical distribution of water vapor in the atmosphere from brightness temperature measurement at frequencies near the 22-GHz line was first investigated theoretically by Barrett and Chung (1962). It was further developed into a technique for determining the excess propagation path by Westwater (1967) and Schaper et al. (1970). To appreciate the degree of correlation between wet path length and brightness temperature, we need to examine the dependence of these quantities on pressure, water vapor density, and temperature. We consider here the interpretation of measurements near the 22.2-GHz resonance. The absorption coefficient given by Eq. (13.42) is complicated, but at line center it can be approximated by

$$\alpha_m \simeq 0.36 \frac{\rho_V}{PT^{1.875}} e^{-644/T} , \tag{13.119}$$

where T is in kelvins, and we have neglected all except the leading terms in Eq. (13.42). We assume that the opacity given by Eq. (13.47) is small, so that the brightness temperature defined by Eq. (13.45) can be written

$$T_B \simeq 17.8 \int_0^\infty \frac{\rho_V}{PT^{0.875}} e^{-644/T} \, dh , \tag{13.120}$$

when we neglect the background temperature T_{B0} and any contributions from clouds. Recall that Eq. (13.16) shows that

$$\mathcal{L}_V = 1763 \times 10^{-6} \int_0^\infty \frac{\rho_V(h)}{T(h)} \, dh . \tag{13.121}$$

Thus, if P and T were constant with height and equal to 1013 mb and 280 K, respectively, we could use Eq. (13.19), $\mathcal{L}_V \simeq 6.3w$, to obtain from Eq. (13.120) the relation $T_B \simeq 12.7w$, where w is the column height of water vapor [see Eq. (13.18)]. Hence, to the degree of approximation used above, we obtain

$$T_B \text{ (22.2 GHz) (K)} \simeq 2.1 \mathcal{L}_V \text{ (cm)} . \tag{13.122}$$

Note that this approximation is valid at sea level. Since, because of pressure broadening, the brightness temperature scales inversely with total pressure [see Eq. (13.120)], the coefficient in Eq. (13.122) is increased to 3.9 for a site at 5000-m elevation, where the pressure is approximately 540 mb. Measurements of brightness temperature and path length estimated from radiosonde profiles show that Eq. (13.122) is a good approximation (see, e.g., Moran and Rosen 1981). Recall that ρ_V is approximately exponentially distributed with a scale height of 2 km. The temperature, on average, decreases by about 2% per kilometer. This change affects the proportionality between T_B and $\mathcal{L}_V$ only through the exponential factor

in Eq. (13.120) and the slight difference in the power law for temperature. Thus, temperature has a small effect. The pressure decreases by 10% per kilometer, so water vapor at higher altitudes contributes more heavily to T_B than is desirable for estimation by radiometry. The sensitivity of T_B to pressure is decreased by moving off the resonance frequency to a frequency near the half-power point of the transition. The reason for this is that as pressure increases, the line profile broadens while the integrated line profile is constant. Therefore, the absorption at line center decreases and the absorption in the line wings increases. Westwater (1967) showed that at 20.6 GHz, the absorption is nearly invariant with pressure. This particular frequency is called the *hinge point*. The opacity at this frequency is less than at the line center, so the nonlinear relationship between T_B and opacity is less important.

The foregoing discussion assumes that measurements of T_B are made in clear-sky conditions. The water droplet content in clouds or fog causes substantial absorption but small change in the index of refraction compared with that of water vapor. Fortunately, the effect of clouds can be eliminated by combining measurements at two frequencies. In nonprecipitating clouds, the sizes of the water droplets are generally less than 100 μm, and at wavelengths greater than a few millimeters, the scattering is small and the attenuation is due primarily to absorption. The absorption coefficient is given by the empirical formula (Staelin 1966)

$$\alpha_{\text{clouds}} \simeq \frac{\rho_L 10^{0.0122(291-T)}}{\lambda^2} \quad (\text{m}^{-1}) \,, \tag{13.123}$$

where ρ_L is the density of liquid water droplets in grams per cubic meter, λ is the wavelength in meters, and T is in kelvins. This formula is valid for λ greater than $\sim$ 3 mm where the droplet sizes are small compared with $\lambda/(2\pi)$. For shorter wavelengths, the absorption is less than predicted by Eq. (13.123) (Freeman 1987; Ray 1972). A very wet cumulus cloud with a water density of 1 g m^{-3} and a size of 1 km will have an absorption coefficient of 7×10^{-5} m^{-1} and will therefore have a brightness temperature of about 20 K at 22 GHz. The index of refraction of liquid water is about 5 at 22 GHz for $T = 280$ K (Goldstein 1951). The actual excess propagation path through the cloud due to liquid water would be about 4 mm, but the predicted excess path from Eq. (13.122) is 10 cm. Thus, the brightness temperature at a single frequency cannot be used reliably to estimate the excess path length when clouds are present. In order to eliminate the brightness temperature contribution of clouds, measurements must be made at two frequencies, ν_1 and ν_2, one near the water line and one well off the water line, respectively. The brightness temperature is

$$T_{Bi} = T_{BVi} + T_{BCi} \,, \tag{13.124}$$

where T_{BVi} and T_{BCi} are the brightness temperatures due to water vapor and clouds at frequency i. Here we neglect the effects of atmospheric O_2. Since, from

Eq. (13.123), $T_{BC} \propto \nu^2$, we can form the observable

$$T_{B1} - T_{B2}\frac{\nu_1^2}{\nu_2^2} = T_{BV1} - T_{BV2}\frac{\nu_1^2}{\nu_2^2} \,, \tag{13.125}$$

which eliminates the effect of clouds. The correlation between $T_{BV1} - T_{BV2} \times \nu_1^2/\nu_2^2$ and $\mathcal{L}_V$ can be estimated from model calculations based on Eqs. (13.45) and (13.16). The off-resonance frequency ν_2 is generally chosen to be about 31 GHz. The problem of finding the two best frequencies and the appropriate correlation coefficients to use in predicting $\mathcal{L}_V$ has been widely discussed (Westwater 1978; Wu 1979; Westwater and Guiraud 1980). The liquid content of clouds can also be measured by dual-frequency techniques [see, e.g., Snider et al. (1980)].

The application of multifrequency microwave radiometry to the calibration of wet path length has been described by Guiraud et al. (1979), Elgered et al. (1982), Resch (1984), Elgered et al. (1991), and Tahmoush and Rogers (2000). A high-performance receiver design is discussed by Tanner and Riley (2003). The results show that $\mathcal{L}_V$ can be estimated to an accuracy better than a few millimeters. This is useful for calibrating VLBI delay measurements and extending coherence times. Measurements of T_B at the antennas of short-baseline interferometers can be useful in correcting the interferometer phase. More accurate predictions of $\mathcal{L}_V$, or interferometer phase, can be obtained by including measurements in other bands. For example, measurements of the wings of the terrestrial oxygen line near 50 GHz can be used to probe the vertical temperature structure of the troposphere [see, e.g., Miner et al. (1972), Snider (1972)]. The accuracy of these schemes has been analyzed by Solheim et al. (1998).

The observation of the 22-GHz line provides a calibration technique that is not sensitive to gain variations and ground pickup. Multiple frequencies can be monitored to correct for clouds and the variable distribution of water vapor with height [see Eq. (13.125)]. For millimeter observations at moderately dry sites, the 22-GHz line may be the best choice [see Bremer (2002) for a description of the system operating at Plateau de Bure]. An example of phase correction based on this line is shown in Fig. 13.20.

13.3.3 183-GHz Water-Vapor Radiometry

For observations at very dry sites, the 183-GHz line may give better results (Lay 1998; Wiedner and Hills 2000). The 183-GHz line is intrinsically about 30 times more sensitive than the 22-GHz line. However, the 183-GHz line is much more easily saturated (i.e., its opacity exceeds unity) than is the 22-GHz line.

A phase-correcting system utilizing the 183-GHz lines was developed for ALMA, and its application is described by Nikolic et al. (2013). Each telescope of

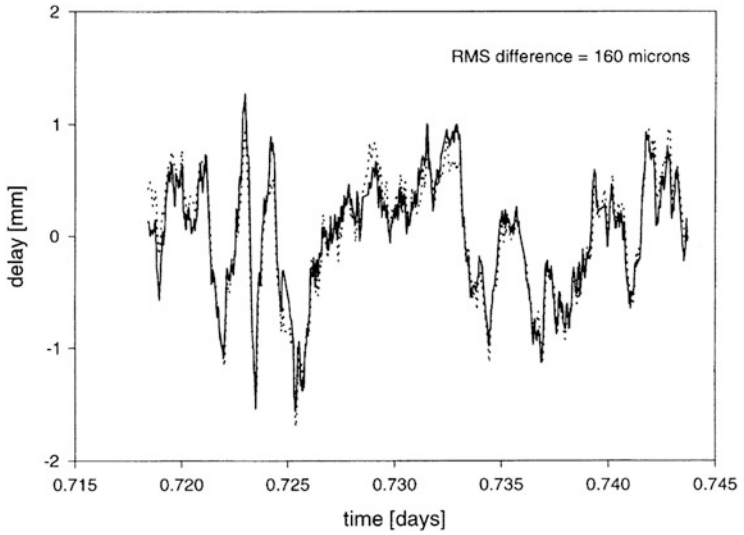

Fig. 13.20 The interferometric phase (in units of delay) measured at 3-mm wavelength on one baseline of the interferometer at Owens Valley Radio Observatory (solid line), and the delay predicted by 22-GHz water-vapor radiometer measurements (dotted line), vs. time. The rms deviation of the difference is 160 μm. The source is 3C273. From Welch (1999), with kind permission from and © URSI; see also Woody et al. (2000).

the array is equipped with a boresighted radiometer having four channels sampling parts of the 183-GHz line profile. The radiometers are double-sideband, and the four channels are symmetrically placed around line center at offsets of 0.5, 3.1, 5.2, and 8.3 GHz. Theoretical line profiles are shown in Fig. 13.21 for various values of precipitable water vapor, w [see Eq. (13.18)]. For low values of w, e.g., 0.3 mm, the maximum sensitivity, dT_B/dw, is obtained at line center. This sensitivity decreases to zero as the line saturates. The channels away from line center become more important as w increases. Combining the measurements with appropriate statistical weights allows accurate estimates of the propagation path over a wide range of conditions. The actual sensitivity coefficients are derived empirically. An example of the reduction in phase noise is shown in Fig. 13.22.

The system does not work well in the presence of clouds, which add a brightness temperature contribution $\sim \nu^2$ [see Eq. (13.123)]. Separate measurements on either side of the line could allow the estimation of the cloud contribution. At low levels of w, an unmodeled contribution to the fluctuations is detected that is attributed to fluctuation in the dry-air component of refractivity. Ancillary measurements of total pressure at each antenna may allow the effects of these fluctuations to be corrected.

The 183-GHz line has been used to estimate w by the atmospheric remote sensing community [e.g., Racette et al. (2005)].

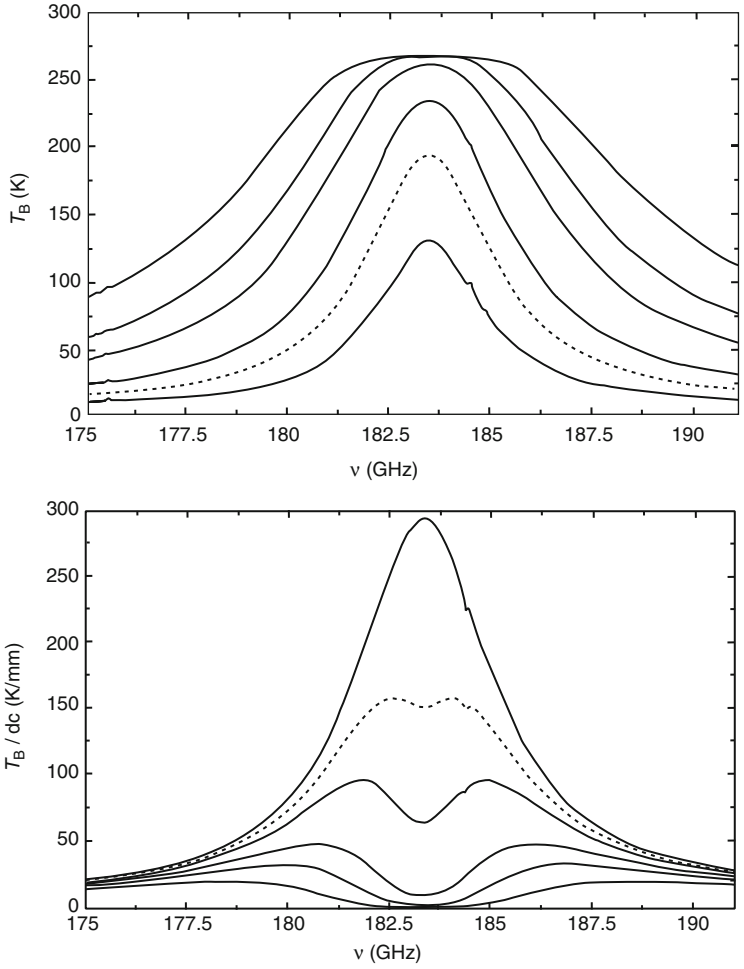

Fig. 13.21 (**top**) Theoretical brightness temperature profiles for the water vapor transition centered at 183.3 GHz appropriate for a site at 5000-m altitude for six values of w, the water vapor column density: (from bottom to top) 0.3, 0.6, 1, 2, 3, and 5 mm. The small blip noticeable at 184.4 GHz is the $10_{0\,10}$–$9_{1\,9}$ ozone transition originating in the upper atmosphere, where pressure broadening is small. The brightness temperature profiles become increasingly saturated at the atmospheric temperature as w increases [see Eq. (13.48)]. (**bottom**) The change of brightness temperature with water vapor column density, dT_B/dw, for the same values of w (from top to bottom). At $w = 5$ mm, the brightness temperature sensitivity to a change in water vapor column density is essentially zero at line center and reaches a broad maximum about 5 GHz from line center. From B. Nikolic et al. (2013), reproduced with permission. © ESO.

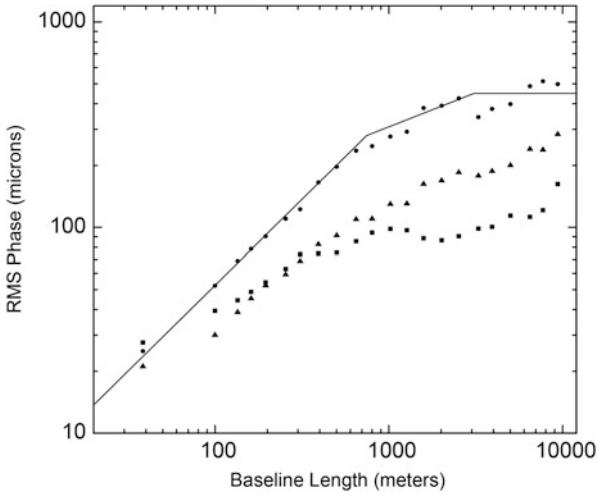

Fig. 13.22 The rms phase (in microns) deviation (square root of the phase structure function, D_ϕ) vs. projected baseline length. Measurements were made on the source 3C138 at 230 GHz in a period of 15 min. The water vapor column density was 1.4 mm, and the surface wind speed was 7 m s^{-1}. The circles show the uncalibrated results. The three-part power law is a suggestive fit to the data. The break at 670 m marks the transition from 3-D to 2-D turbulence and indicates a thickness to the turbulent layer of about 2 km [see Eq. (A13.17)]. The break at 3 km indicates the outer scale of the turbulence. The triangles show the rms phase deviation after water-vapor radiometer corrections. The squares show the rms phase deviations after phase referencing to a calibrator source offset by 1.3° (target/calibrator cycle time was 20 s). Adapted from ALMA Partnership et al. (2015).

13.4 Reduction of Atmospheric Phase Errors by Calibration

Atmospheric phase errors can be treated like antenna-based phase errors in considering their effect on an image. In Sect. 11.4, it is shown that the dynamic range of a snapshot image is approximately

$$\frac{\sqrt{n_a(n_a-1)}}{\phi_{\rm rms}}\ , \tag{13.126}$$

where $\phi_{\rm rms}$ is the rms of the phase error in radians measured with pairs of antennas, and n_a is the number of antennas. For example, if $\phi_{\rm rms}$ is 1 rad and $n_a = 30$, the dynamic range is $\sim$ 30. As a rough guide, the range of $\phi_{\rm rms}$ from 0.5 to 1 rad represents array performance from fair to marginal. The improvement in the image with longer integration depends on the spectrum of the phase fluctuations.

For phase calibration at centimeter wavelengths, it is common to observe a phase calibrator at intervals of $\sim$ 20–30 min. At millimeter wavelengths, this is generally not satisfactory, because of the much greater phase fluctuations resulting from the atmosphere. Procedures that can be used at millimeter and submillimeter wave-

lengths to reduce the effect of atmospheric phase fluctuations are described below. These methods are analogous to those of adaptive optics at optical wavelengths.

Self-Calibration. The simplest way to remove the effects of atmospheric phase fluctuations is to use self-calibration, as described in Sects. 10.3 and 11.3. This method depends on phase closure relationships in groups of three or more antennas. In applying this method, it is necessary to integrate the correlator output data for a long enough time that the source can be detected; that is, the measured visibility phase must result mainly from the source, not the instrumental noise. However, the integration time is limited by the fluctuation rate, so self-calibration is not useful for sources that require long integration times to detect.

Frequent Calibration (Fast Switching). Frequent phase calibration using an unresolved source close to the target source (the source under study) can greatly reduce atmospheric phase errors (Holdaway et al. 1995b; Lay 1997b). To ensure that the atmospheric phase measured on the calibrator is close to that for the target source, the angular distance between the two sources must be no more than a few degrees. The time difference must be less than $\sim$ 1 min, so fast position switching between the target source and the calibrator is required. In the layer in which most of the water vapor occurs, the lines of sight from the antennas to the target source and the calibrator pass within a distance $d_{\rm tc}$ of one another. For a nominal screen height of 1 km, $d_{\rm tc} \simeq 17\theta$, where θ is the angular separation in degrees and $d_{\rm tc}$ is in meters. For one antenna, the rms phase difference between the two paths is $\sqrt{D_\phi(d_{\rm tc})}$ at any instant. If $t_{\rm cyc}$ is the time to complete one observing cycle of the target source and the calibrator, then the mean time difference between the measurements on these two sources is $t_{\rm cyc}/2$. In time $t_{\rm cyc}/2$, the atmosphere will have moved $v_s t_{\rm cyc}/2$. Thus, the phase difference between the measurements on the two paths is effectively $D_\phi(d_{\rm tc} + v_s t_{\rm cyc}/2)$. This is a worst-case estimate, since we have taken the scalar sum of vector quantities corresponding to $d_{\rm tc}$ and v_s. For the difference in the paths to the two antennas as measured by the interferometer, the rms value will be $\sqrt{2}$ times that for one antenna, so the residual atmospheric phase error in the measured visibility is

$$\phi_{\rm rms} = \sqrt{2D_\phi(d_{\rm tc} + v_s t_{\rm cyc}/2)}\ . \tag{13.127}$$

Note that $\phi_{\rm rms}$ is independent of the baseline, so the phase errors should not increase with baseline length. The total time for one cycle of observation of the two sources is the sum of the observing times on the target source and the calibrator, plus twice the antenna slew time between the sources and twice the setup time between ending the slew motion and starting to record data. The observing times required on each of the sources depend on the flux densities and the sensitivity of the instrument. For the calibrator, there may be a choice between a weak source nearby and a stronger one that requires less observing time but more antenna slew time. In order to use calibration sources as a general solution to the atmospheric phase problem, suitable calibrators must be available within a few degrees of any point on the sky. Since calibrator flux densities generally decrease with increasing frequency, it may

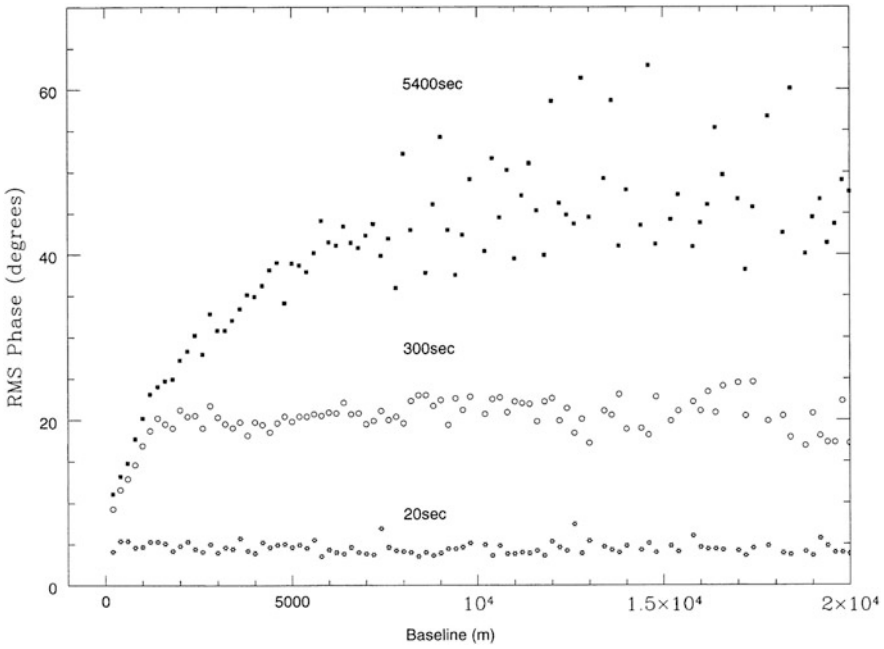

Fig. 13.23 The square root of the phase structure, that is, the rms phase deviation vs. baseline length, for data taken at the VLA at 22 GHz for various averaging times. These data show the effectiveness of fast switching. In these measurements, the target source and calibrator source were the same, 0748+240. The solid squares (labeled 5400 sec) show the rms phase fluctuations with no switching (same data as in Fig. 13.13). The circles and the stars show the rms phase deviation for cycle times 300 s and 20 s, respectively. From Carilli and Holdaway (1999). © 1999 by the American Geophys. Union.

be necessary to observe the calibrator at a lower frequency than is used for the target source. The measured phase for the calibrator must then be multiplied by $\nu_{\rm source}/\nu_{\rm cal}$ (since the troposphere is essentially nondispersive) before subtraction from the target source phases, so the accuracy required for the calibrator phase is increased. Thus, the observing frequency for the calibrator should not be too low; a frequency near 90 GHz may be a practical choice with observations of the target source up to a few hundred gigahertz. The effectiveness of the fast-switching technique is demonstrated by the data in Fig. 13.23. Note that the break in the curve for the 300-s averaging time at antenna spacing 1500 m indicates that the wind speed was about $2\times1500/300 = 10\,{\rm m\,s^{-1}}$ (Carilli and Holdaway 1999). The effectiveness of fast switching for ALMA is described by Asaki et al. (2014).

Paired or Clustered Antennas. Location of antennas in closely spaced pairs is an alternative to fast movement between the target source and the calibrator. One antenna of each pair continuously observes the target source and the other observes the calibrator. With this scheme, $t_{\rm cyc}$ is zero in Eq. (13.127), but the spacing of the paired antennas, d_p, should be included. The rms residual atmospheric error in the

visibility phase becomes

$$\phi_{\rm rms} = \sqrt{2D_\phi(d_{\rm tc} + d_p)}\ . \tag{13.128}$$

As in Eq. (13.127), $\phi_{\rm rms}$ is a worst-case estimate, since we have taken a scalar sum of vector quantities corresponding to $d_{\rm tc}$ and d_p. For a 2° position difference between the target source and the calibrator, and an effective height of 1 km for the water vapor, $d_{\rm tc} = 35$ m. For antennas of diameter ~ 10 m, which is typical for antennas operating up to 300 GHz, d_p should be about 15 m to avoid serious shadowing, and this is smaller than $v_s t_{\rm cyc}/2$ for the fast-switching scheme, since v_s is typically 6–12 m s^{-1} and $t_{\rm cyc}$ is 10 s or more. Thus, with paired antennas, the residual phase errors are somewhat less than with fast switching. Also, observing time is not wasted during antenna slewing and setup. However, with fast switching, about half of the *time* is devoted to the target source, whereas with paired antennas, half of the *antennas* are devoted to the target source, so in the latter case, the sensitivity is less by a factor $\sim \sqrt{2}$. In some cases, the paired antennas are available for use in an array. If the "science array" and the "reference array" are separate, there is no loss of capability in the "science array." Demonstration of the technique for the VLA is described by Carilli and Holdaway (1999) and for the Nobeyama Radio Observatory by Asaki et al. (1996). Another example is the CARMA array of 6-m- and 10-m-diameter antennas. The reference array is comprised of 3.5-m-diameter antennas. This system is described by Peréz et al. (2010) and Zauderer et al. (2016).

Appendix 13.1 Importance of the 22-GHz Line in WWII Radar Development

The history of the 22-GHz transition of water vapor is quite interesting. The water vapor molecule has different moments of inertia about its three axes of rotation, and hence its rotational spectrum is complex, as shown in Fig. A13.1. The rotational energy levels were first determined through measurements of the infrared spectra by Randall et al. (1937). Van Vleck noted in an MIT Radiation Laboratory report (Van Vleck 1942) that these energy levels indicated the existence of an allowable microwave line in the range of 1.2–1.5 cm (20–25 GHz), due to a chance near-coincidence of two energy levels in adjacent rotational ladders. Lying at an energy level of 447 cm^{-1} above the ground state, corresponding to a temperature of 640 K, the line has a Boltzmann population factor at atmospheric temperature that is about 0.1. Van Vleck calculated that atmospheric opacity along horizontal path lengths due to the absorption of H_2O and absorption in the wing of the O_2 lines near 60 GHz would cause problems for radars operating at short centimeter wavelengths. However, there was little empirical data about the pressure-broadening constants for the line widths [see Eq. (13.43) and Fig. 13.7] of these lines, and the estimates Van Vleck used were almost three times larger than than their actual values. Therefore, he substantially overestimated the absorption of O_2 and underestimated the absorption of H_2O at 1.25-cm wavelength. Nonetheless, he raised an important

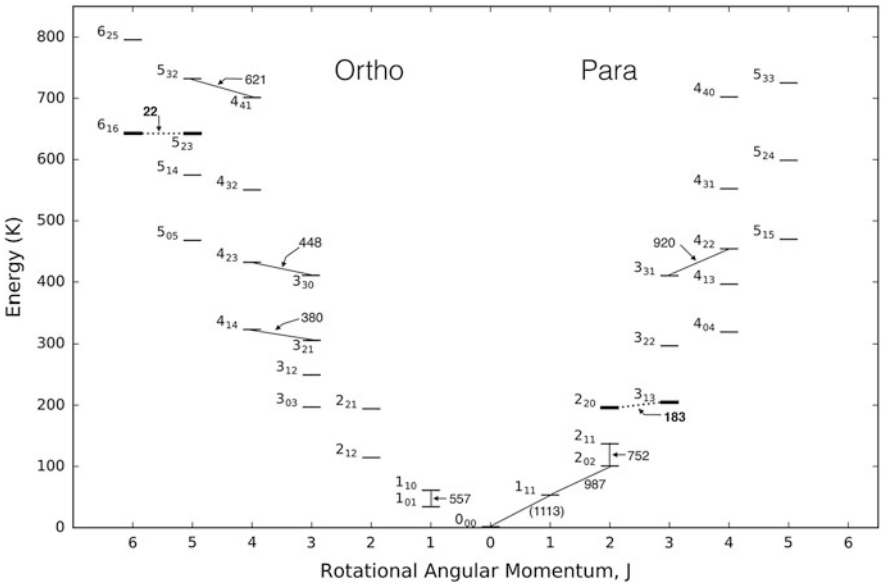

Fig. A13.1 Energy levels of the ground vibrational state of H_2O, an axisymmetric rotating molecule. The quantum numbers are denoted J_{K-1K+1}. $K-1K+1$ are even/odd and odd/even for ortho states and even/even and odd/odd for para states. The seven most important transitions responsible for making the atmosphere opaque at ALMA for a water vapor pressure of 1 mm and frequencies less than 1 THz (see Fig. 13.14) are marked with their frequencies (380, 448, 557, 621, 752, 920, and 987 GHz) along with the ground state transition at 1113 GHz. The diagnostic lines at 22 and 183 GHz used in water-vapor radiometry (Sects. 13.3.2 and 13.3.3) are shown with dotted lines. Other molecular lines causing high opacity are O_2 at 60 GHz and O_3 at 118 GHz. Data from Splatalogue (2016).

concern, which was to go unheeded. His later absorption estimates (Van Vleck 1945, 1947) were more accurate.

Late in World War II, the 3-cm airborne radar had proved to be highly successful. To obtain even higher resolution for antennas of similar size, a new system at 1.25 cm was planned as more powerful microwave signal sources became available. Van Vleck and Townes warned that the new system would have difficulties because of water vapor absorption (see Townes 1952, 1999; Buderi 1996; and Sullivan 2009), but development proceeded nonetheless. The range of the new system, looking along horizontal paths, was found to be only typically 20 km or less, a tremendous disappointment. The cause was quickly traced to atmospheric water vapor absorption. Dicke et al. (1946) traced out the line shape from atmospheric brightness temperature measurements in Florida in 1945 and established the wavelength to be 1.34 cm ($\nu = 22.2$ GHz) and also determined the line profile and absorption coefficient. Planned deployment of the system to the moist South Pacific war zone was canceled. Townes and Merritt (1946) measured the transition at low pressure in the lab to high accuracy ($\nu = 22237 \pm 5$ MHz, 1.349 cm). The

modern standard frequency of the transition, weighted over its hyperfine transitions, is 22235.080 MHz (Kukolich 1969).

Appendix 13.2 Derivation of the Tropospheric Phase Structure Function

The purpose of this appendix is to derive the phase structure function for the troposphere from the structure function for the index of refraction in a turbulent medium. We follow the derivation of Tatarski (1961).

The structure function of phase is defined as

$$D_\phi = \langle [\phi_1(x_1) - \phi_2(x_2)]^2 \rangle \ , \tag{A13.1}$$

where x_1 and x_2 are two measurement points as shown in Fig. A13.2, which for our purposes form a baseline interferometer normal to the incoming propagation direction as viewed outside the homogeneous scattering layer of thickness L. The turbulence is considered to be "frozen" as it moves along the x axis. The ensemble average is usually approximated as a time average of duration T, where T is much longer than the crossing time of the turbulent cells, i.e., $T \gg d/v_s$, where v_s is the wind speed component along the baseline. The initially flat phase front is distorted by the turbulent medium, as shown in the right side of Fig. A13.2. The phase structure function depends only on the separation $d = |x_1 - x_2|$. The structure function of the index of refraction for Kolmogorov turbulence has the general form

$$D_n = C_n^2 \mathbf{r}^{2/3} \ , \tag{A13.2}$$

where $\mathbf{r}$ is the vector separation between two points in the turbulent medium. With the assumption that the medium is isotropic and homogeneous, the structure function becomes a function of only the scalar separation, r,

$$D_n = C_n^2 r^{2/3} \ . \tag{A13.3}$$

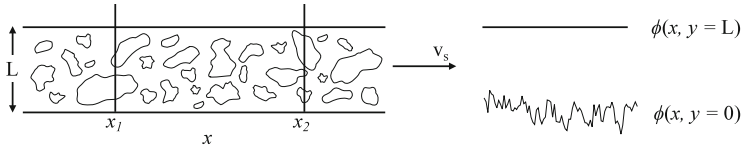

Fig. A13.2 (**left**) Cartoon of a frozen turbulent layer of the troposphere moving along the x axis at velocity v_s. The structure function is measured at two points, x_1 and x_2. (**right**) The incoming signal phase from a point source at the bottom and top of the scattering layer.

From a strict ray-tracing calculation, the phases at some instant will be given by

$$\begin{aligned}\phi_1 &= \frac{2\pi}{\lambda}\int_0^L n(y,x_1)\,dy \\ \phi_2 &= \frac{2\pi}{\lambda}\int_0^L n(y,x_2)\,dy\ ,\end{aligned} \tag{A13.4}$$

where n is the index of refraction along the y axis perpendicular to the baseline, and λ is the wavelength. Except at very dry sites, the fluctuations in refraction are primarily caused by variation in the water vapor density. The difference in phase at points x_1 and x_2 is therefore

$$\phi_1 - \phi_2 = \frac{2\pi}{\lambda}\int_0^L [n(y,x_1) - n(y,x_2)]\,dy\ , \tag{A13.5}$$

and the squared difference of phase is

$$\begin{aligned}(\phi_1 - \phi_2)^2 = \left(\frac{2\pi}{\lambda}\right)^2 &\int_0^L [n(y_a,x_1) - n(y_a,x_2)]\,dy_a \\ &\times \int_0^L [n(y_b,x_1) - n(y_b,x_2)]\,dy_b\ ,\end{aligned} \tag{A13.6}$$

or

$$\begin{aligned}(\phi_1 - \phi_2)^2 = \left(\frac{2\pi}{\lambda}\right)^2 &\int_0^L \int_0^L [n(y_a,x_1) - n(y_a,x_2)] \\ &\times [n(y_b,x_1) - n(y_b,x_2)]\,dy_a\,dy_b\ .\end{aligned} \tag{A13.7}$$

We could expand the integrand in Eq. (A13.7) into cross products of n at different positions. However, we prefer to express the final result in terms of structure functions rather than correlation functions. To proceed, we use the algebraic identity

$$(a-b)(c-d) = \frac{1}{2}[(a-d)^2 + (b-c)^2 - (a-c)^2 - (b-d)^2]\ . \tag{A13.8}$$

Substituting Eq. (A13.7) into Eq. (A13.1), making use of Eq. (A13.8), and taking the expectation term by term, we obtain

$$\begin{aligned}D_\phi(d) = \frac{1}{2}\left(\frac{2\pi}{\lambda}\right)^2 \int_0^L \int_0^L \Big\{ &\langle [n(y_a,x_1) - n(y_b,x_2)]^2 \rangle \\ &+ \langle [n(y_a,x_2) - n(y_b,x_1)]^2 \rangle \\ &- \langle [n(y_a,x_1) - n(y_b,x_1)]^2 \rangle \\ &- \langle [n(y_a,x_2) - n(y_b,x_2)]^2 \rangle \Big\}\, dy_a\,dy_b\ .\end{aligned} \tag{A13.9}$$

The four terms in Eq. (A13.9) are structure functions of the index of refraction for various separations, as defined in Eq. (A13.3). Note that the separation in the first two terms is $[(y_a - y_b)^2 + (x_1 - x_2)^2]^{1/2}$, while the separation in the second two terms is $|y_a - y_b|$. Hence, the structure function of phase can now be written as

$$D_\phi(d) = \left(\frac{2\pi}{\lambda}\right)^2 \int_0^L \int_0^L \left[D_n\left(\sqrt{(y_a - y_b)^2 + (x_1 - x_2)^2}\right) - D_n(|y_a - y_b|)\right] dy_a\, dy_b \,. \tag{A13.10}$$

The integral in Eq. (A13.10) can be simplified because the arguments of D_n are a function of only $y_a - y_b$. Note that an integral of the form

$$I = \int_0^L \int_0^L f(y_a - y_b)\, dy_a\, dy_b \tag{A13.11}$$

can be simplified (see Fig. A13.3) by a change in variables to $y = y_a - y_b$ and y_b. For the case in which $f(y_a - y_b)$ is an even function, Eq. (A13.11) becomes

$$I = 2\int_0^L (L - y) f(y)\, dy \,. \tag{A13.12}$$

By use of this relation, the structure function of phase becomes

$$D_\phi(d) = 2\left(\frac{2\pi}{\lambda}\right)^2 \int_0^L (L - y)\left[D_n\left(\sqrt{y^2 + d^2}\right) - D_n(y)\right] dy \,. \tag{A13.13}$$

Substitution of Eq. (A13.3) into Eq. (A13.13) gives

$$D_\phi(d) = 2\left(\frac{2\pi}{\lambda}\right)^2 C_n^2 \int_0^L (L - y)[(y^2 + d^2)^{1/3} - y^{2/3}]\, dy \,. \tag{A13.14}$$

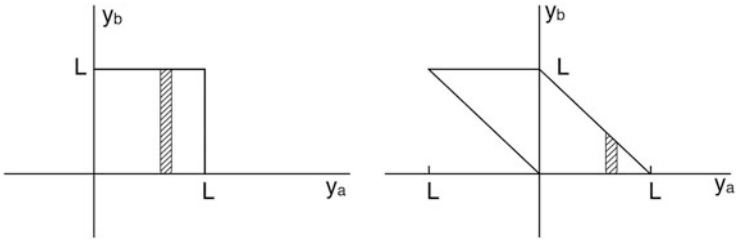

Fig. A13.3 The change in integration variables from y_a, y_b to y, y_b, where $y = y_a - y_b$ for the derivation of Eq. (A13.12).

This equation is the general starting point for most discussions (see Tatarski 1961, eq. 6.27). The distinction of two major regimes, $d \ll L$ and $d \gg L$, was first made in the context of radio interferometry by Stotskii (1973, 1976) and further discussed by Dravskikh and Finkelstein (1979) and Coulman (1990).

The case $d \ll L$ is called the "three-dimensional," or 3-D, turbulence solution. The integral in Eq. (A13.14) is maximum at $y = 0$, where it equals $L\,d^{2/3}$ and decreases monotonically to zero as y increases. It declines slowly for $y < d$, and for larger y, it decreases as $y^{-4/3}$. Hence, the integrand is approximately constant in the range of y from 0 to d, and most of the contribution to the integral is within this range. Thus, from Eq. (A13.14), $D_\phi \sim L\,d^{2/3} \times d \sim L\,d^{5/3}$. The proportionality constant, as reported by Tatarski (1961, eq. 6.65), based on analytic approximation, is about 2.91. Hence,

$$D_\phi(d) = 2.91 \left(\frac{2\pi}{\lambda}\right)^2 C_n^2 L\, d^{5/3} , \qquad d_f, d_{\text{in}} < d \ll L . \tag{A13.15}$$

The case $d \gg L$ is called the "two-dimensional," or 2-D, turbulence case. Stotskii (1973) and Coulman (1990) presented the reasons why Eq. (A13.14), strictly valid for isotropic turbulence, can be used for this case. When $d \gg L$, the argument in brackets in Eq. (A13.14) becomes $\sim d^{2/3} - y^{2/3}$, and Eq. (A13.14) can be integrated directly. The leading term in the integral is $\frac{1}{2}L^2 d^{2/3}$, which gives

$$D_\phi(d) \simeq \left(\frac{2\pi}{\lambda}\right)^2 C_n^2 L^2 d^{2/3} , \qquad L \ll d < L_{\text{out}} . \tag{A13.16}$$

For $d > L_{\text{out}}$, D_n becomes independent of distance, and D_ϕ becomes flat.

It is interesting to note that the two structure functions given in Eqs. (A13.15) and (A13.16) intersect at a distance

$$d_2 = L/2.9 , \tag{A13.17}$$

which can be taken to be the nominal transition point from 3-D to 2-D turbulence. For a scale height of 2 km, this would be about 700 m. Numerical integrations of Eq. (A13.14) have been done by Treuhaft and Lanyi (1987). An example of such an integration is shown in Fig. A13.4. Note that the transition from the 2-D to 3-D structure functions is rather gradual. This probably explains why large variations in the power-law index have been reported from observational data.

The results described above can be generalized for the case in which the propagation angle is not normal to the baseline but rather is at an angle y. In this situation, L is replaced by $L \sec y$ for a plane-parallel atmosphere. Thus, Eqs. (A13.15) and (A13.16) show that the structure functions vary as $\sec y$ and $\sec^2 y$ for the 3-D and 2-D cases, respectively.

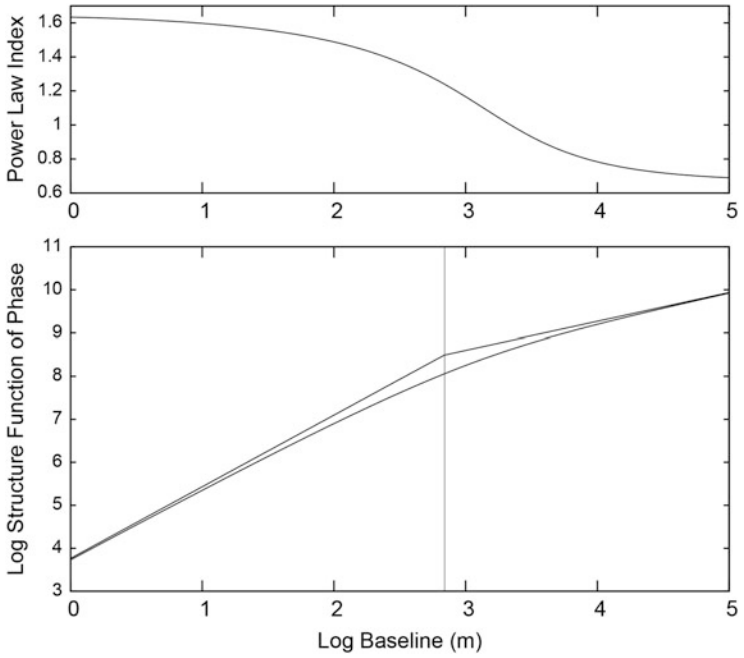

Fig. A13.4 (**bottom**) Structure function of phase vs. baseline length (d) and its power-law approximations for a layer thickness of 2 km and turbulence parameter $C_n^2 = 1$. The intersection of the two power-law components, which occurs at $d = L/2.9 = d_2$, or about 700 m, is marked by the thin vertical line. (**top**) Power-law index as a function of baseline for the structure function of phase.

Further Reading

Andrews, D.G., *An Introduction to Atmospheric Physics*, Cambridge Univ. Press, Cambridge, UK (2000)

Baldwin, J.E. and Wang, S., Eds., *Radio Astronomical Seeing*, International Academic Publishers and Pergamon Press, Oxford, UK (1990)

Janssen, M.A., *Atmospheric Remote Sensing by Microwave Radiometry*, Wiley, New York (1993)

Mangum, J.G., and Wallace, P., Atmospheric Refractive Electromagnetic Wave Bending and Propagation Delay, *Pub. Astron. Soc. Pacific*, **127**, 74–91, (2015)

Proc. RadioNet Workshop on Measurement of Atmospheric Water Vapour: Theory, Techniques, Astronomical, and Geodetic Applications, Wettzell/Hoellenstein, Germany, Oct. 9–11 (2006). http://bit.ly/1Knb11E

Tatarski, V.I., *Wave Propagation in a Turbulent Medium*, Dover, New York (1961)

Westwater, R., Ed., *Specialist Meeting on Microwave Radiometry and Remote Sensing Applications*, National Oceanic and Atmospheric Administration, U.S. Dept. Commerce (1992)

References

ALMA Partnership, Fomalont, E.B., Vlahakis, C., Corder, S., Remijan, A., Barkats, D., Lucas, R., Hunter, T.R., Brogan, C.L., Asaki, Y., and 239 coauthors, The 2014 ALMA Long Baseline Campaign: An Overview, *Astrophys. J. Lett.*, **808**, L1 (11 pp) (2015)

Altenhoff, W.J., Baars, J.W.M., Downes, D., and Wink, J.E., Observations of Anomalous Refraction at Radio Wavelengths, *Astron. Astrophys.*, **184**, 381–385 (1987)

Andrews, D.G., *An Introduction to Atmospheric Physics*, Cambridge Univ. Press, Cambridge, UK (2000), p. 24.

Armstrong, J.W., and Sramek, R.A., Observations of Tropospheric Phase Scintillations at 5 GHz on Vertical Paths, *Radio Sci.*, **17**, 1579–1586 (1982)

Asaki, Y., Matsushita, S., Kawabe, R., Fomalont, E., Barkats, D., and Corder, S., ALMA Fast Switching Phase Calibration on Long Baselines, in *Ground-Based and Airborne Telescopes V*, L. M. Stepp, R. Gilmozzi, and H. J. Hall, Eds., Proc. SPIE, **9145**, 91454K-1 (2014)

Asaki, Y., Saito, M., Kawabe, R., Morita, K.-I., and Sasao, T., Phase Compensation Experiments with the Paired Antennas Method, *Radio Sci.*, **31**, 1615–1625 (1996)

Baars, J.W.M., Meteorological Influences on Radio Interferometer Phase Fluctuations, *IEEE Trans. Antennas Propag.*, **AP-15**, 582–584 (1967)

Barrett, A.H., and Chung, V.K., A Method for the Determination of High-Altitude Water-Vapor Abundance from Ground-Based Microwave Observations, *J. Geophys. Res.*, **67**, 4259–4266 (1962)

Battat, J.B., Blundell, R., Moran, J.M., and Paine, S., Atmospheric Phase Correction Using Total Power Radiometry at the Submillimeter Array, *Astrophys. J. Lett.*, **616**, L71–L74 (2004)

Bean, B.R., and Dutton, E.J., *Radio Meteorology*, National Bureau of Standards Monograph 92, U.S. Government Printing Office, Washington, DC (1966)

Beaupuits, J.P.P., Rivera, R.C., and Nyman, L.-A., Height and Velocity of the Turbulence Layer at Chajnantor Estimated from Radiometric Measurements, ALMA Memo 542 (2005)

Bevis, M., Businger, S., Chiswell, S., Herring, T.A., Anthes, R.A., Rocken, C., and Ware, R.H., GPS Meteorology: Mapping Zenith Wet Delays onto Precipitable Water, *J. Appl. Meteor.*, **33**, 379–386 (1994)

Bieging, J.H., Morgan, J., Welch, W.J., Vogel, S.N., Wright, M.C.H., Interferometer Measurements of Atmospheric Phase Noise at 86 GHz, *Radio Sci.*, **19**, 1505–1509 (1984)

Bohlander, R.A., McMillan, R.W., and Gallagher, J.J., Atmospheric Effects on Near-Millimeter-Wave Propagation, *Proc. IEEE*, **73**, 49–60 (1985)

Bolton, R., Nikolic, B., and Richer, J., The Power Spectrum of Atmospheric Path Fluctuations at the ALMA Site from Water Vapour Radiometer Observations, ALMA Memo 592 (2011)

Bracewell, R.N., *The Fourier Transform and Its Applications*, 3rd ed., McGraw-Hill, New York (2000) (earlier eds. 1965, 2000).

Bremer, M., Atmospheric Phase Correction for Connected-Element Interferometry and for VLBI, in *Astronomical Site Evaluation in the Visible and Radio Range*, J. Vernin, Z. Benkhaldoun, and C. Muñoz-Tuñón, Eds., Astron. Soc. Pacific Conf. Ser., **266**, 238–245 (2002)

Buderi, R., *The Invention That Changed the World*, Simon and Schuster, New York (1996), pp. 261 and 340.

Butler, B., Precipitable Water at the VLA—1990–1998, MMA Memo 237, National Radio Astronomy Observatory (1998)

Butler, B., and Desai, K., Phase Fluctuations at the VLA Derived from One Year of Site Testing Interferometer Data, VLA Test Memo 222, National Radio Astronomy Observatory (1999)

Butler, B.J., Radford, S.J.E., Sakamoto, S., Kohno, K., Atmospheric Phase Stability at Chajnantor and Pampa la Bola, ALMA Memo 365 (2001)

Calisse, P.G., Ashley, M.C.B., Burton, M.G., Phillips, M.A., Storey, J.W.V., Radford, S.J.E., and Peterson, J.B., Submillimeter Site Testing at Dome C, Antarctica, *Pub. Astron. Soc. Austr.*, **21**, 256–263 (2004)

Carilli, C.L., and Holdaway, M.A., Tropospheric Phase Calibration in Millimeter Interferometry, *Radio Sci.*, **34**, 817–840 (1999)

Chamberlin, R.A., and Bally, J., The Observed Relationship Between the South Pole 225-GHz Atmospheric Opacity and the Water Vapor Column Density, *Int. J. Infrared and Millimeter Waves*, **16**, 907–920 (1995)

Chamberlin, R.A., Lane, A.P., and Stark, A.A., The 492 GHz Atmospheric Opacity at the Geographic South Pole, *Astrophys. J.*, **476**, 428–433 (1997)

Chylek, P., and Geldart, D.J.W., Water Vapor Dimers and Atmospheric Absorption of Electromagnetic Radiation, *Geophys. Res. Lett.*, **24**, 2015–2018 (1997)

COESA, *U.S. Standard Atmosphere, 1976*, NOAA-S/T 76-1562, U.S. Government Printing Office, Washington, DC (1976)

Coulman, C.E., Fundamental and Applied Aspects of Astronomical "Seeing," *Ann. Rev. Astron. Astrophys.*, **23**, 19–57 (1985)

Coulman, C.E., Atmospheric Structure, Turbulence, and Radioastronomical "Seeing," in *Radio Astronomical Seeing*, J. E. Baldwin and S. Wang, Eds., International Academic Publishers and Pergamon Press, Oxford, UK (1990), pp. 11–20.

Coulman, C.E., Tropospheric Phenomena Responsible for Anomalous Refraction at Radio Wavelengths, *Astron. Astrophys.*, **251**, 743–750 (1991)

Cox, A.N., Ed., *Allen's Astrophysical Quantities*, 4th ed., AIP Press, Springer, New York (2000), Sec. 11.20, p. 262.

Crane, R.K., Refraction Effects in the Neutral Atmosphere, in *Methods of Experimental Physics*, Vol. 12, Part B *(Astrophysics: Radio Telescopes)*, Meeks, M.L., Ed., Academic Press, New York (1976), pp. 186–200.

Crane, R.K., Fundamental Limitations Caused by RF Propagation, *Proc. IEEE*, **69**, 196–209 (1981)

Davis, J.L., Herring, T.A., Shapiro, I.I., Rogers, A.E.E., and Elgered, G., Geodesy by Radio Interferometry: Effects of Atmospheric Modeling Errors on Estimates of Baseline Length, *Radio Sci.*, **20**, 1593–1607 (1985)

Debye, P., *Polar Molecules*, Dover, New York (1929)

Delgado, G., Otárola, A., Belitsky, V., and Urbain, D., The Determination of Precipitable Water Vapour at Llano de Chajnantor from Observations of the 183 GHz Water Line, ALMA Memo 271 (1998)

Dicke, R.H., Beringer, R., Kyhl, R.L., and Vane, A.B., Atmospheric Absorption Measurements with a Microwave Radiometer, *Phys. Rev.*, **70**, 340–348 (1946)

Downes, D., and Altenhoff, W.J., Anomalous Refraction at Radio Wavelengths, in *Radio Astronomical Seeing*, Baldwin, J.E., and Wang, S., Eds., International Academic Publishers and Pergamon Press, Oxford, UK (1990), pp. 31–40.

Dravskikh, A.F., and Finkelstein, A.M., Tropospheric Limitations in Phase and Frequency Coordinate Measurements in Astronomy, *Astrophys. Space Sci.*, **60**, 251–265 (1979)

Elgered, G., Davis, J.L., Herring, T.A., and Shapiro, I.I., Geodesy by Radio Interferometry: Water Vapor Radiometry for Estimation of the Wet Delay, *J. Geophys. Res.*, **96**, 6541–6555 (1991)

Elgered, G., Rönnäng, B.O., and Askne, J.I.H., Measurements of Atmospheric Water Vapor with Microwave Radiometry, *Radio Sci.*, **17**, 1258–1264 (1982)

Freeman, R.L., *Radio System Design for Telecommunications (1–100 GHz)*, Wiley, New York (1987)

Fried, D.L., Statistics of a Geometric Representation of Wavefront Distortion, *J. Opt. Soc. Am.*, **55**, 1427–1435 (1965)

Fried, D.L., Optical Resolution Through a Randomly Inhomogeneous Medium for Very Long and Very Short Exposures, *J. Opt. Soc. Am.*, **56**, 1372–1379 (1966)

Fried, D.L., Optical Heterodyne Detection of an Atmospherically Distorted Signal Wave Front, *Proc. IEEE*, **55**, 57–67 (1967)

Goldstein, H., Attenuation by Condensed Water, in *Propagation of Short Radio Waves*, MIT Radiation Laboratory Ser., Vol. 13, Kerr, D.E., Ed., McGraw-Hill, New York (1951), pp. 671–692.

Grischkowsky, D., Yang, Y., and Mandehgar, M., Zero-Frequency Refractivity of Water Vapor: Comparison of Debye and Van Vleck–Weisskopf Theory, *Optics Express*, **21**, 18899–18908 (2013)

Guiraud, F.O., Howard, J., and Hogg, D.C., A Dual-Channel Microwave Radiometer for Measurement of Preciptable Water Vapor and Liquid, *IEEE Trans. Geosci. Electron.*, **GE-17**, 129–136 (1979)

Hess, S.L., *Introduction to Theoretical Meteorology*, Holt, Rinehart, Winston, New York (1959)

Hill, R.J., Water Vapor-Absorption Line Shape Comparison Using the 22-GHz Line: The Van Vleck–Weisskopf Shape Affirmed, *Radio Sci.*, **21**, 447–451 (1986)

Hill, R.J., and Clifford, S.F., Contribution of Water Vapor Monomer Resonances to Fluctuations of Refraction and Absorption for Submillimeter through Centimeter Wavelengths, *Radio Sci.*, **16**, 77–82 (1981)

Hill, R.J., Lawrence, R.S., and Priestley, J.T., Theoretical and Calculational Aspects of the Radio Refractive Index of Water Vapor, *Radio Sci.*, **17**, 1251–1257 (1982)

Hills, R.E., Webster, A.S., Alston, D.A., Morse, P.L.R., Zammit, C.C., Martin, D.H., Rice, D.P., and Robson, E.I., Absolute Measurements of Atmospheric Emission and Absorption in the Range 100–1000 GHz, *Infrared Phys.*, **18**, 819–825 (1978)

Hinder, R.A., Observations of Atmospheric Turbulence with a Radio Telescope at 5 GHz, *Nature*, **225**, 614–617 (1970)

Hinder, R.A., Fluctuations of Water Vapour Content in the Troposphere as Derived from Interferometric Observations of Celestial Radio Sources, *J. Atmos. Terr. Phys.*, **34**, 1171–1186 (1972)

Hinder, R.A., and Ryle, M., Atmospheric Limitations to the Angular Resolution of Aperture Synthesis Radio Telescopes, *Mon. Not. R. Astron. Soc.*, **154**, 229–253 (1971)

Hogg, D.C., Guiraud, F.O., and Sweezy, W.B., The Short-Term Temporal Spectrum of Precipitable Water Vapor, *Science*, **213**, 1112–1113 (1981)

Holdaway, M.A., Ishiguro, M., Foster, S.M., Kawabe, R., Kohno, K., Owen, F.N., Radford, S.J.E., and Saito, M., Comparison of Rio Frio and Chajnantor Site Testing Data, MMA Memo 152, National Radio Astronomy Observatory (1996)

Holdaway, M.A., Radford, S.J.E., Owen, F.N., and Foster, S.M., Data Processing for Site Test Interferometers, ALMA Memo 129 (1995a)

Holdaway, M.A., Radford, S.J.E., Owen, F.N., and Foster, S.M., Fast Switching Phase Calibration: Effectiveness at Mauna Kea and Chajnantor, MMA Memo 139, National Radio Astronomy Observatory (1995b)

Holdaway, M.A., and Woody, D., Yet Another Look at Anomalous Refraction, MMA Memo 223, National Radio Astronomy Observatory (1998)

Ishiguro, M., Kanzawa, T., and Kasuga, T., Monitoring of Atmospheric Phase Fluctuations Using Geostationary Satellite Signals, in *Radio Astronomical Seeing*, Baldwin, J.E., and Wang, S., Eds., International Academic Publishers and Pergamon Press, Oxford, UK (1990), pp. 60–63

Jackson, J.D., *Classical Electrodynamics*, 3rd ed., Wiley, New York (1999), pp. 775–784

Kasuga, T., Ishiguro, M., and Kawabe, R., Interferometric Measurement of Tropospheric Phase Fluctuations at 22 GHz on Antenna Spacings of 27 to 540 m, *IEEE Trans. Antennas Propag.*, **AP-34**, 797–803 (1986)

Kimberk, R.S., Hunter, T.R., Leiker, P.S., Blundell, R., Nystrom, G.U., Petitpas, G.R., Test, J., Wilson, R.W., Yamaguchi, P., and Young, K.H., A Multi-Baseline 12 GHz Atmospheric Phase Interferometer with One Micron Path Length Sensitivity, *J. Astron. Inst.*, **1**, 1250002 (2012)

Kukolich, S.G., Measurement of the Molecular g Values in H_2O and D_2O and Hyperfine Structure in H_2O, *J. Chem. Phys.*, **50**, 3751–3755 (1969)

Lamb, J.W., and Woody, D., Radiometric Correction of Anomalous Refraction, MMA Memo 224, National Radio Astronomy Observatory (1998)

Lay, O.P., The Temporal Power Spectrum of Atmospheric Fluctuations Due to Water Vapor, *Astron. Astrophys. Suppl.*, **122**, 535–545 (1997a)

Lay, O.P., Phase Calibration and Water Vapor Radiometry for Millimeter-Wave Arrays, *Astron. Astrophys. Suppl.*, **122**, 547–557 (1997b)

Lay, O.P., 183 GHz Radiometric Phase Correction for the Millimeter Array, MMA Memo 209, National Radio Astronomy Observatory (1998)

Lichtenstein, M., and Gallagher, J.J., Millimeter Wave Spectrum of Ozone, *J. Molecular Spectroscopy*, **40**, 10–26 (1971)

Liebe, H.J., Calculated Tropospheric Dispersion and Absorption Due to the 22-GHz Water Vapor Line, *IEEE Trans. Antennas Propag.*, **AP-17**, 621–627 (1969)

Liebe, H.J., Modeling Attenuation and Phase of Radio Waves in Air at Frequencies below 1000 GHz, *Radio Sci.*, **16**, 1183–1199 (1981)

Liebe, H.J., An Updated Model for Millimeter Wave Propagation in Moist Air, *Radio Sci.*, **20**, 1069–1089 (1985)

Liebe, H.J., MPM: An Atmospheric Millimeter-Wave Propagation Model, *Int. J. Infrared and Millimeter Waves*, **10**, 631–650 (1989)

Loudon, R., *The Quantum Theory of Light*, 2nd ed., Oxford Univ. Press, London (1983)

Marini, J.W., Correction of Satellite Tracking Data for an Arbitrary Tropospheric Profile, *Radio Sci.*, **7**, 223–231 (1972)

Masson, C.R., Atmospheric Effects and Calibrations, in *Astronomy with Millimeter and Submillimeter Wave Interferometry*, Ishiguro, M., and Welch, W.J., Eds., Astron. Soc. Pacific Conf. Ser., **59**, 87–95 (1994a)

Masson, C.R., Seeing, in *Very High Angular Resolution Imaging*, IAU Symp. 158, Robertson, J.G., and Tango, W.J., Eds., Kluwer, Dordrecht, the Netherlands (1994b), pp. 1–10

Matsushita, S., Matsuo, H., Pardo, J.R., and Radford, S.J.E., FTS Measurements of Submillimeter-Wave Atmospheric Opacity at Pampa la Bola II: Supra-Terahertz Windows and Model Fitting, *Pub. Ast. Soc. Japan*, **51**, 603–610 (1999)

Matsushita, S., Matsuo, H., Wiedner, M.C., and Pardo, J.R., Phase Correction Using Submillimeter Atmospheric Continuum Emission, ALMA Memo 415 (2002)

Millenaar, R.P., Tropospheric Stability at Candidate SKA Sites: Australia Edition, SKA Doc. WP3-040.020.001-TR-003 (2011a)

Millenaar, R.P., Tropospheric Stability at Candidate SKA Sites: South Africa Edition, SKA Doc. WP3-040.020.001-TR-002 (2011b)

Miner, G.F., Thornton, D.D., and Welch, W.J., The Inference of Atmospheric Temperature Profiles from Ground-Based Measurements of Microwave Emission from Atmospheric Oxygen, *J. Geophys. Res.*, **77**, 975–991 (1972)

Morabito, D.D., D'Addario, L.R., Acosta, R.J., and Nessel, J.A., Tropospheric Delay Statistics Measured by Two Site Test Interferometers at Goldstone, California, *Radio Sci.*, **48**, 1–10 (2013)

Moran, J.M., and Rosen, B.R., Estimation of the Propagation Delay through the Troposphere from Microwave Radiometer Data, *Radio Sci.*, **16**, 235–244 (1981)

Niell, A.E., Global Mapping Functions for the Atmospheric Delay at Radio Wavelengths, *J. Geophys Res.*, **101**, 3227–3246 (1996)

Nikolic, B., Bolton, R.C., Graves, S.F., Hills, R.E., and Richter, J.S., Phase Collection for ALMA with 183 GHz Water Vapour Radiometers, *Astron. Astrophys.*, **552**, A104 (11pp) (2013)

Olmi, L., and Downes, D., Interferometric Measurement of Tropospheric Phase Fluctuations at 86 GHz on Antenna Spacings of 24 m to 288 m, *Astron. Astrophys.*, **262**, 634–643 (1992)

Owens, J.C., Optical Refractive Index of Air: Dependence on Pressure, Temperature, and Composition, *Appl. Opt.*, **6**, 51–58 (1967)

Paine, S., The *am* Atmospheric Model, SMA Technical Memo 152, Smithsonian Astrophysical Observatory, Cambridge, MA (2016)

Paine, S., Blundell, R., Papa, D.C., Barrett, J.W., and Radford, S.J.E., A Fourier Transform Spectrometer for Measurement of Atmospheric Transmission at Submillimeter Wavelengths, *Publ. Astron. Soc. Pacific*, **112**, 108–118 (2000)

Pardo, J.R., Cernicharo, J., and Serabyn, E., Atmospheric Transmission at Microwaves (ATM): An Improved Model for Millimeter/Submillimeter Applications, *IEEE Trans. Antennas Propag.*, **49**, 1683–1694 (2001a)

Pardo, J.R., Serabyn, E., and Cernicharo, J., Submillimeter Atmospheric Transmission Measurements on Mauna Kea During Extremely Dry El Niño Conditions, *J. Quant. Spect. Rad. Trans.*, **68**, 419–433 (2001b)

Peixoto, J.P., and Oort, A.H., The Climatology of Relative Humidity in the Atmosphere, *J. Climate*, **9**, 3443–3463 (1996)

Peréz, L.M., Lamb, J.W., Woody, D.P., Carpenter, J.M., Zauderer, B.A., Isella, A., Bock, D.C., Bolatto, A.D., Carlstrom, J., Culverhouse, T.L., and nine coauthors, Atmospheric Phase Correction Using CARMA-PACs: High-Angular-Resolution Observations of the Fu Orionis Star PP 13S*, *Astrophys. J.*, **724**, 493–501 (2010)

Pol, S.L.C., Ruf, C.S., and Keihm, S.J., Improved 20- to 32-GHz Atmospheric Absorption Model, *Radio Sci.*, **33**, 1319–1333 (1998)

Racette, P.E., Westwater, E.R., Han, Y., Gasiewski, A.J., Klein, M., Cimini, D., Jones, D.C., Manning, W., Kim, E.J., Wang, J.R., Leuski, V., and Kiedron, P., Measurement of Low Amounts of Precipitable Water Vapor Using Ground-Based Millimeter-Wave Radiometry, *J. Atmos. Oceanic Tech.*, **22**, 317–337 (2005)

Radford, S.J.E., and Peterson, J.B., Submillimeter Atmospheric Transparency at Maunakea, at the South Pole, and at Chajnantor, *Publ. Astron. Soc. Pacific*, **128**:075001 (13pp) (2016)

Radford, S.J.E., Reiland, G., and Shillue, B., Site Test Interferometer, *Publ. Astron. Soc. Pacific*, **108**, 441–445 (1996)

Randall, H.M., Dennison, D.M., Ginsburg, N., and Weber, L.R., The Far Infrared Spectrum of Water Vapor, *Phys. Rev.*, **52**, 160–174 (1937)

Ray, P.S., Broadband Complex Refractive Indices of Ice and Water, *Applied Optics*, **11**, 1836–1843 (1972)

Reber, E.E., and Swope, J.R., On the Correlation of Total Precipitable Water in a Vertical Column and Absolute Humidity, *J. Appl. Meteor.*, **11**, 1322–1325 (1972)

Resch, G.M., Water Vapor Radiometry in Geodetic Applications, in *Geodetic Refraction: Effects of Electromagnetic Wave Propagation Through the Atmosphere*, Brunner, F.K., Ed., Springer-Verlag, Berlin (1984), pp. 53–84

Rienecker, M.M., Suarez, M.J., Gelaro, R., Todling, R., Bacmeister, J., Liu, E., Bosilovich, M.G., Schubert, S.D., Takacs, L., Kim, G.-K., and 19 coauthors, MERRA: NASA's Modern Era Retrospective Analysis for Research and Applications, *J. Climate*, **24**, 3624–3648 (2011)

Roddier, F., The Effects of Atmospheric Turbulence in Optical Astronomy, in *Progress in Optics XIX*, E. Wolf, Ed., North-Holland, Amsterdam (1981), pp. 281–376

Rogers, A.E.E., and Moran, J.M., Coherence Limits for Very-Long-Baseline Interferometry, *IEEE Trans. Instrum. Meas.*, **IM-30**, 283–286 (1981)

Rogers, A.E.E., Moffet, A.T., Backer, D.C., and Moran, J.M., Coherence Limits in VLBI Observations at 3-MillimeterWavelength, *Radio Sci.*, **19**, 1552–1560 (1984)

Rosenkranz, P.W., Water Vapor Microwave Continuum Absorption: A Comparison of Measurements and Models, *Radio Sci.*, **33**, 919–928 (1998)

Rüeger, J.M., Refractive Indices of Light, Infrared, and Radio Waves in the Atmosphere, Unisurv Report S-68, School of Surveying and Spatial Information Systems, University of New South Wales, Sydney, Australia (2002)

Rybicki, G.B., and Lightman, A.P., *Radiative Processes in Astrophysics*, Wiley-Interscience, New York (1979) (reprinted 1985)

Saastamoinen, J., Introduction to Practical Computation of Astronomical Refraction, *Bull. Géodésique*, **106**, 383–397 (1972a)

Saastamoinen, J., Atmospheric Correction for the Troposphere and Stratosphere in Radio Ranging of Satellites, in *The Use of Artificial Satellites for Geodesy*, Geophys. Monograph 15, American Geophysical Union, Washington, DC (1972b), pp. 247–251

Schaper, Jr. L.W., Staelin, D.H., and Waters, J.W., The Estimation of Tropospheric Electrical Path Length by Microwave Radiometry, *Proc. IEEE*, **58**, 272–273 (1970)

Sims, G., Kulesa, C., Ashley, M.C.B., Lawrence, J.S., Saunders, W., and Storey, J.W.V., Where is Ridge A?, in *Ground-Based and Airborne Telescopes IV*, Proc. SPIE, **8444**, 84445H-1–84445H-9 (2012)

Smart, W.M., *Textbook on Spherical Astronomy*, 6th ed., revised by R. M. Green, Cambridge Univ. Press, Cambridge, UK (1977)

Smith, Jr. E.K., and Weintraub, S., The Constants in the Equation for Atmospheric Refractive Index at Radio Frequencies, *Proc. IRE*, **41**, 1035–1037 (1953)

Snider, J.B., Ground-Based Sensing of Temperature Profiles from Angular and Multi-Spectral Microwave Emission Measurements, *J. Appl. Meteor.*, **11**, 958–967 (1972)

Snider, J.B., Burdick, H.M., and Hogg, D.C., Cloud Liquid Measurement with a Ground-Based Microwave Instrument, *Radio Sci.*, **15**, 683–693 (1980)

Solheim, F., Godwin, J.R., Westwater, E.R., Han, Y., Keihm, S.J., Marsh, K., and Ware, R., Radiometric Profiling of Temperature, Water Vapor, and Cloud Liquid Water Using Various Inversion Methods, *Radio Sci.*, **33**, 393–404 (1998)

Sramek, R., VLA Phase Stability at 22 GHz on Baselines of 100 m to 3 km, VLA Test Memo 143, National Radio Astronomy Observatory (1983)

Sramek, R.A., Atmospheric Phase Stability at the VLA, in *Radio Astronomical Seeing*, Baldwin, J.E., and Wang, S., Eds., International Academic Publishers and Pergamon Press, Oxford, UK (1990), pp. 21–30

Staelin, D.H., Measurements and Interpretation of the Microwave Spectrum of the Terrestrial Atmosphere near 1-Centimeter Wavelength, *J. Geophys. Res.*, **71**, 2875–2881 (1966)

Stotskii, A.A., Concerning the Fluctuation Characteristics of the Earth's Troposphere, *Radiophys. and Quantum Elect.*, **16**, 620–622 (1973)

Stotskii, A.A., Tropospheric Limitations of the Measurement Accuracy on Coordinates of Cosmic Radio Source, *Radiophys. and Quantum Elect.*, **19**, 1167–1169 (1976)

Sullivan,W.T., III, *Cosmic Noise: A History of Early Radio Astronomy*, Cambridge Univ. Press, Cambridge, UK (2009)

Sutton, E.C., and Hueckstaedt, R.M., Radiometric Monitoring of Atmospheric Water Vapor as It Pertains to Phase Correction in Millimeter Interferometry, *Astron. Astrophys. Suppl.*, **119**, 559–567 (1996)

Sutton, E.C., Subramanian, S., and Townes, C.H., Interferometric Measurements of Stellar Positions in the Infrared, *Astron. Astrophys.* **110**, 324–331 (1982)

Tahmoush, D.A., and Rogers, A.E.E., Correcting Atmospheric Variations in Millimeter Wavelength Very Long Baseline Interferometry Using a Scanning Water Vapor Radiometer, *Radio Sci.*, **35**, 1241–1251 (2000)

Tanner, A.B., and Riley, A.L., Design and Performance of a High-Stability Water Vapor Radiometer, *Radio Sci.*, **38**, 8050 (17pp) (2003)

Tatarski, V.I., *Wave Propagation in a Turbulent Medium*, Dover, New York (1961)

Tatarski, V.I., *The Effects of the Turbulent Atmosphere on Wave Propagation*, National Technical Information Service, Springfield, VA (1971)

Taylor, G.I., Spectrum of Turbulence, *Proc. R. Soc. London A*, **164**, 476–490 (1938)

Thayer, G.D., An Improved Equation for the Radio Refractive Index of Air, *Radio Sci.*, **9**, 803–807 (1974)

Toll, J.S., Causality and the Dispersion Relation: Logical Foundations, *Phys. Rev.*, **104**, 1760–1770 (1956)

Townes, C.H., Microwave Spectroscopy, *Am. Scientist*, **40**, 270–290 (1952)

Townes, C.H., *How the Laser Happened*, Oxford Univ. Press, Oxford, UK (1999), p. 40

Townes, C.H., and Merritt, F.R., Water Spectrum Near One-Centimeter Wave-Length, *Phys. Rev.*, **70**, 558–559 (1946)

Treuhaft, R.N., and Lanyi, G.E., The Effect of the Dynamic Wet Troposphere on Radio Interferometric Measurements, *Radio Sci.*, **22**, 251–265 (1987)

Van Vleck, J.H., *Atmospheric Absorption of Microwaves*, MIT Radiation Laboratory Report 43-2 (1942)

Van Vleck, J.H., Further Theoretical Investigations of the Atmospheric Absorption of Microwaves, MIT Radiation Laboratory Report 664 (1945)

Van Vleck, J.H., The Absorption of Microwaves by Uncondensed Water Vapor, *Phys. Rev.*, **71**, 425–433 (1947)

Van Vleck, J.H., Purcell, E.M., and Goldstein, H., Atmospheric Attenuation, in *Propagation of Short Radio Waves*, MIT Radiation Laboratory Ser., Vol. 13, D. E. Kerr, Ed., McGraw-Hill, New York (1951), pp. 641–692

Waters, J.W., Absorption and Emission by Atmospheric Gases, in *Methods of Experimental Physics*, Vol. 12, Part B *(Astrophysics: Radio Telescopes)*, Meeks, M.L., Ed., Academic Press, New York (1976), pp. 142–176

Welch, W.J., Correcting Atmospheric Phase Fluctuations by Means of Water-Vapor Radiometry, in *The Review of Radio Science, 1996–1999*, Stone, W.R., Ed., Oxford Univ. Press, Oxford, UK (1999), pp. 787–808

Westwater, E.R., *An Analysis of the Correction of Range Errors Due to Atmospheric Refraction by Microwave Radiometric Techniques*, ESSA Technical Report IER 30-ITSA 30, Institute for Telecommunication Sciences and Aeronomy, Boulder, CO (1967)

Westwater, E.R., The Accuracy of Water Vapor and Cloud Liquid Determination by Dual-Frequency Ground-Based Microwave Radiometry, *Radio Sci.*, **13**, 677–685 (1978)

Westwater, E.R., and Guiraud, F.O., Ground-Based Microwave Radiometric Retrieval of Precipitable Water Vapor in the Presence of Clouds with High Liquid Content, *Radio Sci.*, **15**, 947–957 (1980)

Wiedner, M.C., and Hills, R.E., Phase Correction on Mauna Kea Using 183 GHz Water Vapor Monitors, in *Imaging at Radio through Submillimeter Wavelengths*, Mangum, J.G., and Radford, S.J.E., Eds., Astron. Soc. Pacific Conf. Ser., **217**, 327–335 (2000)

Woody, D., Carpenter, J., and Scoville, N., Phase Correction at OVRO Using 22 GHz Water Line, in *Imaging at Radio through Submillimeter Wavelengths*, Mangum, J.G., and Radford, S.J.E., Eds., Astron. Soc. Pacific Conf. Ser., **217**, 317–326 (2000)

Woolf, N.J., High Resolution Imaging from the Ground, *Ann. Rev. Astron. Astrophys.*, **20**, 367–398 (1982)

Wright, M.C.H., Atmospheric Phase Noise and Aperture-Synthesis Imaging at Millimeter Wavelengths, *Publ. Astron. Soc. Pacific*, **108**, 520–534 (1996)

Wright, M.C.H., and Welch, W.J., Interferometer Measurements of Atmospheric Phase Noise at 3 mm, in *Radio Astronomical Seeing*, Baldwin, J.E., and Wang, S., Eds., International Academic Publishers and Pergamon Press, Oxford, UK (1990), pp. 71–74

Wu, S.C., Optimum Frequencies of a Passive Microwave Radiometer for Tropospheric Path-Length Correction, *IEEE Trans. Antennas Propag.*, **AP-27**, 233–239 (1979)

Zauderer, B.A., Bolatto, A.D., Vogel, S.N., Carpenter, J.M., Peréz, L.M., Lamb, J.W., Woody, D.P., Bock, D.C.-J., Carlstrom, J.E., Culverhouse, T.L., and 12 coauthors, The CARMA Paired Antenna Calibration System: Atmospheric Phase Correction for Millimeter-Wave Interferometry and Its Application to Mapping the Ultraluminous Galaxy Arp 193, *Astron. J.*, **151**, 18 (19pp) (2016)

Zivanovic, S.S., Forster, J.R., and Welch, W.J., A New Method for Improving the Interferometric Resolution by Compensating for the Atmospherically Induced Phase Shift, *Radio Sci.*, **30**, 877–884 (1995)